

LOCALIZED PLASMON-COUPLED  
SEMICONDUCTOR NANOCRYSTAL  
EMITTERS FOR INNOVATIVE  
DEVICE APPLICATIONS

A THESIS  
SUBMITTED TO THE DEPARTMENT OF ELECTRICAL AND  
ELECTRONICS ENGINEERING  
AND THE INSTITUTE OF ENGINEERING AND SCIENCES  
OF BILKENT UNIVERSITY  
IN PARTIAL FULLFILMENT OF THE REQUIREMENTS  
FOR THE DEGREE OF  
MASTER OF SCIENCE

By  
İbrahim Murat Soğancı

August 2007

I certify that I have read this thesis and that in my opinion it is fully adequate, in scope and in quality, as a thesis for the degree of Master of Science.

---

Assist. Prof. Dr. Hilmi Volkan Demir (Supervisor)

I certify that I have read this thesis and that in my opinion it is fully adequate, in scope and in quality, as a thesis for the degree of Master of Science.

---

Assist. Prof. Dr. Vakur B. Ertürk

I certify that I have read this thesis and that in my opinion it is fully adequate, in scope and in quality, as a thesis for the degree of Master of Science.

---

Assist. Prof. Dr. Dönüş Tuncel

Approved for the Institute of Engineering and Sciences:

---

Prof. Dr. Mehmet B. Baray  
Director of Institute of Engineering and Sciences

ABSTRACT

LOCALIZED PLASMON-COUPLED  
SEMICONDUCTOR NANOCRYSTAL EMITTERS  
FOR INNOVATIVE DEVICE APPLICATIONS

İbrahim Murat Soğancı

M.S. in Electrical and Electronics Engineering

**Supervisor:** Assist. Prof. Dr. Hilmi Volkan Demir

August 2007

Quantum confinement allows for the development of novel luminescent materials such as colloidal semiconductor quantum dots for a variety of photonic applications spanning from biomedical labeling to white light generation. However, such device applications require efficient photoluminescence. To this end, in this thesis we investigate the spontaneous emission characteristics of semiconductor nanocrystal emitters under different conditions and their enhancement and controlled modification via plasmonic resonance coupling, placing metallic nanoparticles in their proximity, for innovative device applications. We first present our theoretical and experimental work on the optical characterization of nanocrystals (e.g., CdSe, CdS, and CdSe/ZnS) including absorption/photoluminescence, time-resolved luminescence, and excitation spectra measurements. Here we demonstrate very strong electromodulation (up to 90%) of photoluminescence and absorption of such nanocrystals (nanodots and nanorods) for optical modulator applications. Second, we present our electromagnetic modeling on the optical response of metal nanoparticles using finite-difference-time-domain method. For the first time, using localized plasmons of metal nanoisland films (nano-silver) carefully spectrally and spatially tuned for optimal coupling conditions, we report very significant controlled modifications of nanocrystal emission including the peak

emission wavelength shift (by 14nm), emission linewidth reduction (by 10nm with 22% FWHM reduction), photoluminescence intensity enhancement (15.1- and 21.6-fold compared to the control groups of the same nanocrystals with no plasmonic coupling and those with identical nano-silver but no dielectric spacer in the case of non-radiative energy transfer, respectively), and selectable peaking of surface-state emission at desired wavelengths. Such localized plasmonic engineering of nanocrystal emitters opens new possibilities for our light-emitting and photovoltaic devices.

*Keywords:* Quantum confinement, quantum dots, nanocrystals, nanorods, spontaneous emission, photoluminescence, electromodulation, metal nanoparticles, localized plasmons, metal-enhanced luminescence, FDTD.

ÖZET

YENİLİKÇİ AYGIT UYGULAMALARI İÇİN  
LOKAL PLAZMON KATKILI  
YARIİLETKEN NANOKRİSTAL IŞIYICILAR

İbrahim Murat Soğancı

Elektrik ve Elektronik Mühendisliği Bölümü Yüksek Lisans

Tez Yöneticisi: Yrd. Doç. Dr. Hilmi Volkan Demir

Ağustos 2007

Kuantum sınırlandırma, koloidal yarıiletken kuantum noktaları gibi ışıyıcı malzemelerin biyomedikal görüntüleme beyaz ışık üretimine kadar uzanan çeşitli fotonik uygulamalar için kullanılmasını olanaklı kılmaktadır. Sözü edilen aygıt uygulamaları verimli fotoışma gerektirmektedir. Bu amaçla, bu tez çalışmasında yarıiletken nanokristallerin kendiliğinden ışınalım özelliklerini değişik koşullarda inceledik ve yenilikçi aygıt uygulamaları için yakınlarına metal nanoparçacıklar yerleştirerek plazmon rezonans etkisiyle artışını ve denetimli değişikliğini sağladık. Öncelikle, nanokristallerin (örneğin CdSe, CdS ve CdSe/ZnS) soğurma/fotoışma, zaman-çözümlü ışma ve uyarma tayfi ölçümlerini içeren optik karakterizasyonu üzerine kuramsal ve deneysel çalışmalarımızı sunduk. Optik kipleyci uygulamaları için, nanokristallerde (nano-noktalar ve nano-çubuklar) çok güçlü (% 90'a kadar) fotoışma ve soğurma elektro-kiplmesi gösterdik. Ardından, zamanda sonlu farklar (FDTD) yöntemiyle metal nanoparçacıkların optik yanıtı üzerine elektromanyetik modellememizi sunduk. İlk defa, metal nano-ada filmlerin (nano-gümüş) lokal plazmonlarını uzaysal ve spektral olarak optimum optik etkileşim için tasarlayıp kullanarak, ışma doruk dalgaboyu kayması (14 nm), ışma eğrisi daralması (yarı yükseklikteki tam genişlikte % 22'ye denk gelen 10 nm'lik daralma), fotoışma şiddet artışı (aynı nanokristallerin plazmonik etkileşim olmadığı ve aynı nanokristaller ile aynı nano-gümüş arasında dielektrik katman olmadığı

durumlara göre sırasıyla 15.1 ve 21.6 kat) ve yüzey ışımalarının istenilen dalgaboyunda seçilmiş doruklandırılması gibi nanokristal ışımaları ile ilgili çarpıcı değişiklikleri deneysel olarak gerçekleştirdik. Bu tez çalışmasında nanokristallerin bu şekilde lokal plazmon mühendisliği, ışık yayan ve fotovoltaik aygıtlarımız için yeni olanaklar sunmaktadır.

*Anahtar sözcükler:* Kuantum sınırlandırma, kuantum noktaları, nanokristaller, nano-çubuklar, kendiliğinden ışınım, fotoışım, elektro-kiplleme, metal nanoparçacıklar, lokal plazmonlar, metalle artırılan ışım, zamanda sonlu farklar (FDTD).

# Acknowledgements

I would like to express my gratitude to my supervisor, Asst. Prof. Dr. Hilmi Volkan Demir for his supervision and support from the beginning to the end of my master's study. With his wisdom and personality, he is a model for my academic future.

I would like to thank the members of my thesis committee, Asst. Prof. Dr. Vakur B. Ertürk and Asst. Prof. Dr. Dönüş Tuncel for their useful comments and suggestions.

I would like to thank Prof. Dr. Ekmel Özbay for the facilities at Nanotechnology Research Center. Without those equipments, it would be impossible to accomplish this experimental research work.

I would like to thank our research partner Dr. Sergey Gaponenko at the Institute of Atomic and Molecular Physics of Belarus for providing me their characterization equipments and great hospitality for two weeks.

I would like to thank Evren Mutlugün, Sedat Nizamoğlu, Emre Ünal, Onur Akın, Emre Sarı, Dr. Nihan Kosku Perkgöz, Özgün Akyüz, Sümeyra Tek, İlkem Özge Huyal, Tuncay Özel, Can Uran, Aslı Koç, Gülis Zengin, and Rohat Melik from Demir Group and Bayram Bütün, Turgut Tut, Deniz Çalışkan, Erkin Ülker, Evrim Çolak and Atilla Özgür Çakmak from Özbay Group for their invaluable support.

I would also like to thank my family for making it possible to achieve my goals since my childhood.

Finally, I would like to acknowledge the financial support of TÜBİTAK (Scientific and Technological Research Foundation of Turkey) as a scholarship during my master's study.

# Table of Contents

<b>ACKNOWLEDGEMENTS.....</b>	<b>VII</b>
<b>1. INTRODUCTION.....</b>	<b>1</b>
<b>2. SURFACE PLASMONS .....</b>	<b>5</b>
2.1 SURFACE PLASMON POLARITONS.....	5
2.1.1 <i>Physical Explanation</i> .....	5
2.1.2 <i>Excitation of Surface Plasmon Polaritons</i> .....	7
2.1.3 <i>Field Enhancement</i> .....	10
2.2 LOCALIZED SURFACE PLASMONS.....	11
2.2.1 <i>Physical Explanation</i> .....	11
2.2.2 <i>Parameters Affecting Resonance Conditions</i> .....	14
2.2.2.1 <i>Size</i> .....	14
2.2.2.2 <i>Shape</i> .....	15
2.2.2.3 <i>Material</i> .....	15
2.2.2.4 <i>Medium Properties</i> .....	16
2.3 ELECTROMAGNETIC SIMULATION OF LOCALIZED SURFACE PLASMONS.....	16
2.3.1 <i>The Finite-Difference Time-Domain Method</i> .....	16
2.3.2 <i>Implementation</i> .....	18
2.3.3 <i>Results</i> .....	25
<b>3. SEMICONDUCTOR NANOCRYSTALS.....</b>	<b>35</b>
3.1 THEORY.....	35
3.1.1 <i>Definition and Basics</i> .....	35
3.1.2 <i>Energy States in Quantum Dots</i> .....	36
3.1.3 <i>Broadening mechanisms</i> .....	39
3.2 EXPERIMENTAL CHARACTERIZATION.....	41
3.2.1 <i>Nanocrystal Processing Techniques</i> .....	41
3.2.2 <i>Optical Absorption and Emission Measurements</i> .....	42
3.2.3 <i>Electromodulation of Optical Properties of CdSe Nanorod and Nanodot Films</i> .....	47
<b>4. LOCALIZED PLASMON-COUPLED EMISSION OF NANOCRYSTALS.....</b>	<b>53</b>
4.1 METAL-ENHANCED LUMINESCENCE.....	53
4.2 METAL NANOSTRUCTURES PREPARATION.....	57
4.3 EXPERIMENTAL DEMONSTRATION OF LOCALIZED PLASMON-COUPLED EMISSION FROM NANOCRYSTALS.....	63
4.3.1 <i>Plasmon-Coupled Emission of CdSe/ZnS Nanocrystals</i> .....	63
4.3.2 <i>Plasmon-Engineered Emission of Surface State-Emitting Nanocrystals</i> .....	70
<b>5. CONCLUSION.....</b>	<b>72</b>

# List of Figures

Figure 1. 1 Representative cross section of a core-shell nanocrystal with surfactants (ligands) at the outermost surface (after [1]).....	2
Figure 2.1.1. 1 Surface charges and electric field distribution perpendicular to the surface. Also, the magnetic field is depicted (after [10]) .....	6
Figure 2.1.1. 2 Comparison of dispersion relations of surface plasmon polariton modes at a metal-dielectric interface and photons in the same dielectric medium (after [12]). .....	7
Figure 2.1.2. 1 Scattering of electrons in the metal film (a), and the position of the corresponding wave vector on the surface on the dispersion curve (after [11]). .....	8
Figure 2.1.2. 2 Reflection of light at a metal-dielectric boundary. Medium 1 is metal and medium 2 is air or vacuum (after [11]).....	9
Figure 2.1.2. 3 Comparison of wave vector of light with an angle of incidence of $\theta_0$ in free space (1) , in medium 0 (2), with the dispersion relation graph of surface plasmon polaritons at medium 1-medium 2 interface (after [11]). .....	10
Figure 2.2.1. 1 Real and imaginary components of the dielectric constant of silver plotted as a function of photon energy. The width of the curves represents the amount of experimental error (after [16]). .....	13
Figure 2.3.1. 1 Yee cell .....	18
Figure 2.3.2. 1 Real (a) and imaginary (b) parts of the dielectric permittivity of silver plotted using Drude model .....	20
Figure 2.3.3. 1 Diagram representing the simulation region.....	26
Figure 2.3.3. 2 The comparison of electric field amplitude at the surface of the nanosphere in longitudinal axis and without the presence of silver nanosphere at the same location when excited at 390 nm free-space wavelength (the unit of x-axis is seconds and the unit of y-axis is arbitrary). .....	27

Figure 2.3.3. 3 The comparison of electric field amplitude at a distance of 0.8 nm from the surface of the silver nanosphere in longitudinal axis and without the silver nanosphere at the same location when excited at 390 nm free-space wavelength (the unit of x-axis is seconds and the unit of y-axis is arbitrary).....	28
Figure 2.3.3. 4 The comparison of electric field amplitude at a distance of 1.6 nm from the surface of the silver nanosphere in longitudinal axis and without the silver nanosphere at the same location when excited at 390 nm free-space wavelength (the unit of x-axis is seconds and the unit of y-axis is arbitrary).....	29
Figure 2.3.3. 5 The comparison of electric field amplitude at the surface of the silver nanosphere in transverse axis and without the silver nanosphere at the same location when excited at 390 nm free-space wavelength (the unit of x-axis is seconds and the unit of y-axis is arbitrary).....	30
Figure 2.3.3. 6 The comparison of electric field amplitude at a distance of 0.8 nm from the surface of the silver nanosphere in transverse axis and without the silver nanosphere at the same location when excited at 390 nm free-space wavelength (the unit of x-axis is seconds and the unit of y-axis is arbitrary).....	31
Figure 2.3.3. 7 The comparison of electric field amplitude at a distance of 1.6 nm from the surface of the silver nanosphere in transverse axis and without the silver nanosphere at the same location when excited at 390 nm free-space wavelength (the unit of x-axis is seconds and the unit of y-axis is arbitrary).....	32
Figure 2.3.3. 8 Enhanced electromagnetic field intensity distribution with respect to distance from the surface with a $1/r^6$ -dependence (the unit of x-axis is nm and the unit of y-axis is arbitrary).....	33
Figure 2.3.3. 9 Spectral distribution of electric field amplitude at the surface of silver nanocylinder (the unit of x-axis is nm and the unit of y-axis is arbitrary).....	34
Figure 3.1.3. 1 Evolution of the optical absorption spectrum of semiconductor nanocrystals with full-width at half-maximum enlarging with increasing size distribution in the ensemble (after [32]).....	40
Figure 3.2.2. 1 Absorption and photoluminescence spectra of CdSe/ZnS core-shell nanocrystals with diameters of 2.1 nm (a), 2.7 nm (b), and 5.3 nm (c). .....	44

Figure 3.2.2. 2 Photoluminescence excitation and photoluminescence spectra of CdSe/ZnS nanocrystals with peak emission wavelength of 623 nm (a) and 585 nm (b). .....	45
Figure 3.2.2. 3 Time-resolved photoluminescence of CdSe/Zns core-shell nanocrystals with emission wavelengths of 585 nm (a) and 620 nm (b). ..	47
Figure 3.2.3. 1 Photoluminescence spectra of CdSe nanorods film under different applied voltages. Inset shows the integrated PL intensity vs. the applied electric field. ....	49
Figure 3.2.3. 2 Differential PL (a) and normalized differential PL (b) spectra of CdSe nanorods vs. applied electric field. ....	50
Figure 3.2.3. 3 Optical density of CdSe nanodots for different electric field values.....	51
Figure 3.2.3. 4 Photoluminescence of CdSe nanodots for different electric field values.....	52
Figure 3.2.3. 5 Differential photoluminescence spectra of CdSe nanodots under different applied electric fields.....	52
Figure 4.1. 1 Distance dependence of the three mechanisms (quenching, increased field, and increased rate) caused by metal-luminophore interaction (after [43]) .....	55
Figure 4.2. 1 SEM images of our silver nanoisland films: (a) 20 nm mass thickness, not annealed, (b) 20 nm mass thickness, annealed at 300 °C for 10 min., (c) 6 nm mass thickness, annealed at 150°C for 1 min., and (d) 2 nm mass thickness, annealed at 150°C for 2 min. ....	58
Figure 4.2. 2 Optical absorption spectra of silver nanoislands with mass thickness of 4 nm annealed at 300°C for 20 min, nano-silver (2 nm) at 150 °C for 2 min, nano-silver (6 nm) at 150°C for 2 min, and nano-silver (6 nm) at 150 °C for 2 min covered with 10 nm thick Si <sub>x</sub> O <sub>y</sub> film. ....	59
Figure 4.2. 3 Optical absorption spectrum of a gold island film with a mass thickness of 4 nm annealed at 300 °C for 10 minutes. ....	61
Figure 4.2. 4 Optical absorption spectrum of a silver-gold alloy metal island film. The mass thicknesses of silver and gold are 2 nm, the annealing temperature is 300 °C, and the annealing duration is 10 minutes. ....	62

Figure 4.3.1. 1 Schematic view of the two types of samples prepared: a 10 nm thick silicon oxide film between metal island films and nanocrystals (a), and nanocrystals directly on metal island film (b). .....	65
Figure 4.3.1. 2 Optical absorption spectra of Ag (20 nm) annealed at 300 °C for 10 min and that also covered with 10 nm-thick Si <sub>x</sub> O <sub>y</sub> along with the photoluminescence spectrum of CdSe/ZnS nanocrystals.....	66
Figure 4.3.1. 3 Photoluminescence peak intensity of CdSe/ZnS nanocrystals with silver (20 nm) and a dielectric spacer (10 nm silicon oxide) between them is 15.1 times larger than that of the same CdSe/ZnS nanocrystals alone and 21.6 times stronger than that of the same CdSe/ZnS nanocrystals with identical silver nanoislands (20 nm) but no dielectric spacer. ....	67
Figure 4.3.1. 4 Photoluminescence peak wavelength of CdSe/ZnS nanocrystals+Si <sub>x</sub> O <sub>y</sub> +nanoAg (506 nm) is shifted by 14 nm with respect to CdSe/ZnS nanocrystals alone (492 nm) due to plasmonic resonance coupling. Their FWHM linewidth is also narrowed by 10 nm due to the plasmon coupling. ....	68
Figure 4.3.1. 5 Electroluminescence spectrum of the LED with CdSe/ZnS core-shell nanocrystals close to silver island films (a), and of the same sample (with no metal structures) isolated from any plasmon coupling (b).....	69
Figure 4.3.2. 1 Photoluminescence spectrum of surface state emitting CdS nanocrystals. ....	70
Figure 4.3.2. 2 Photoluminescence spectrum of surface state emitting nanocrystals without the influence of plasmons compared with those of the same material close to silver and gold nanoislands with the plasmonic coupling. ....	71

# List of Tables

Table 4.2. 1Average silver nanoisland diameter for different deposition conditions .....	59
Table 4.2. 2Localized plasmon resonance wavelengths of metal island films under different fabrication and measurement conditions. ....	63

# Chapter 1

## Introduction

In recent years, significant scientific research has been performed on semiconductor and metal nanoparticles especially because of their interesting optical characteristics, which are not observed in bulk materials. Carrier and photon confinement in such semiconductor and metal nanoparticles under certain circumstances (i.e., resonance conditions) is the reason of these different optical characteristics. As a result of these peculiar optical properties, the use of such nanoparticles in photonic device applications is promising to obtain better performances by modifying currently available devices and to invent new ones with novel functionality.

Nanocrystals have crystalline structure (periodic stacking of atoms), but consist of nanometer-size clusters, with diameters comparable to the exciton Bohr radius and the de Broglie electron wavelength, and are distinctly separated from each other. Among the examples of such semiconductor nanocrystals are those from II-VI, III-V and VI-VI Groups. Colloidal nanocrystals are chemically synthesized, and their sizes and formations are controlled through chemical reaction parameters. Figure 1.1 presents a representative cross-section of a core-shell nanocrystal. The electron confinement in nanocrystals, i.e., the quantum confinement, leads to discretization of energy levels, making major changes in the energy spectrum of electronic excitation and probability of optical transitions (thus the optical absorption and emission spectra). Therefore, the bandgap energy of the nanocrystals is size-dependent and both their absorption edge and peak emission wavelength can be tuned within a certain spectral range

conveniently by controlling their crystal size. Both optical absorption and emission processes are efficient in these quantum-confined structures. For example, the luminescence quantum efficiency of II-VI Group nanocrystals may be very high, in some cases as high as 80 % at room temperature [2]. Because of all these interesting optical properties, nanocrystals have great potential to be used in new optical and optoelectronic devices. The ability to fine-tune their optical properties using size effect is the most important advantage of nanocrystals, making it possible to increase the performance of existing devices, and even facilitate to implement new functions. Our research activities are focused on the quantum mechanical and electromagnetic mechanisms to engineer the optical processes taking place in nanocrystals. To this end, in this thesis we investigate the optical properties of different nanocrystals (made of CdSe, CdS and CdSe/ZnS) modified in a controlled manner under different conditions (e.g., under electric field, with plasmonic resonance coupling) for innovative device applications.

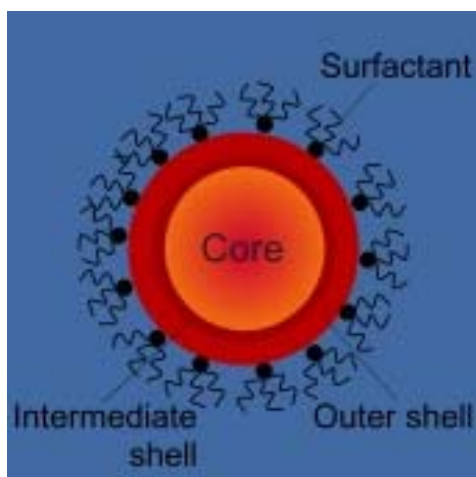


**Figure 1. 1 Representative cross section of a core-shell nanocrystal with surfactants (ligands) at the outermost surface (after [1]).**

Surface plasmons are the collective oscillations of conduction band electrons at the surfaces of metal films or in metal nanoparticles. The technical term of “propagating surface plasmons” (and sometimes only “surface plasmons”) is used for plasmons on continuous metal surfaces and the term of “localized

surface plasmons” (and “particle plasmons”) is used for plasmons in metal nanoparticles and metal nanostructures. Plasmons can be optically excited if the optical frequency and wave vector of the incident photons match those of the plasmons. At specific resonance frequencies, plasmon modes generate very large amplitudes of electron oscillations. Around the resonance frequencies, the local electromagnetic field in the vicinity of the electron oscillations may be very high, which we prove by solving Maxwell’s equations using the finite-difference time-domain method. The interplay between plasmons and photons make very interesting applications possible, including surface-enhanced Raman scattering [3], plasmon-enhanced nonlinear optical processes [4], plasmon-enhanced two-photon absorption [5], and metal-enhanced fluorescence [6]. Similar interactions between plasmonic metal nanoparticles and nanocrystal emitters also exhibit such interesting results, and in this thesis we investigate the localized plasmonic engineering of the nanocrystal photoemission experimentally. Considering the spatial and spectral conditions of strong plasmon-nanocrystal interactions, we design, fabricate and characterize metallic nanostructures. These results prove to be promising, with significant enhancement in the luminescence intensity, shift in the peak emission wavelength and narrowing in the emission linewidth. This opens new opportunities for device applications as also suggested and experimented.

The organization of this thesis is as follows: In Chapter 2 we introduce surface plasmons. In this chapter, the physical explanation of surface plasmons and localized plasmons is provided; their optical excitation methods, the spatial and spectral distribution of the electromagnetic fields in their vicinity and the effects of particle and structure properties on resonance conditions are explained. Here we also provide our electromagnetic simulations of the field distribution around metal nanospheres under different excitation conditions. Chapter 3 focuses on semiconductor nanocrystals. This chapter includes theoretical explanation of the optical properties of semiconductor nanocrystals, description of experimental techniques for nanocrystal film preparation, and their optical characterization under different conditions (e.g., under electric

field). In Chapter 4, plasmon-material interactions are included. The physical interactions leading to metal-enhanced fluorescence are discussed; our experimental method of producing metal nanostructures is presented with the systematic study of fabrication conditions; our design for the optimization of metal-nanocrystal interactions is presented; significant modification in the emission characteristics of nanocrystals in our fabricated structures are demonstrated; and our device applications of such plasmon-coupled nanocrystal emitters are introduced with experiment results.

# Chapter 2

## Surface Plasmons

Surface plasmon is a quantum of collective oscillations of conduction band electrons in metals [7]. The oscillations of these negatively charged carriers are accompanied with electromagnetic fields. The boundary conditions of the electromagnetic fields accompanying electron oscillations on metal surfaces and in metal nanoparticles are different. This leads to different physical solutions to these two situations known as surface plasmons for on-surface oscillations and localized plasmons for in-nanoparticle oscillations.

### 2.1 Surface Plasmon Polaritons

#### 2.1.1 Physical Explanation

The existence of surface plasmon oscillations on metal-dielectric boundaries was demonstrated by *Powell* and *Swan* using electron energy-loss experiments [8]. These oscillations on metal-dielectric boundaries bring together electromagnetic fields in close proximity to the surface. Such electromagnetic excitations bounded to the free charges on conductor surfaces are named as polaritons [9], and the whole phenomenon including the surface plasma waves and the accompanying fields is called as surface plasmon polaritons. Figure 2.1.1.1

displays the electrons at a metal-dielectric interface and the spatial distribution of the accompanying fields.

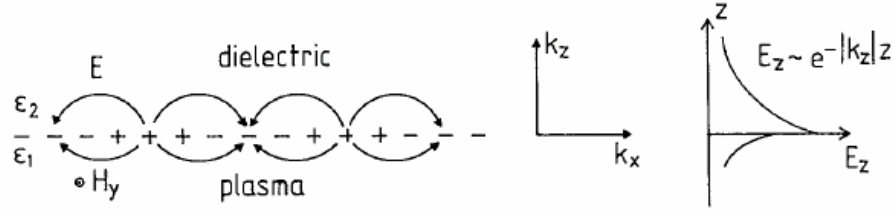


**Figure 2.1.1. 1 Surface charges and electric field distribution perpendicular to the surface. Also, the magnetic field is depicted (after [10])**

Assuming that there is no dependence in the y-axis, the electric field distribution of a surface polariton propagating on the x direction as in Figure 2.1.1.1 is as follows:

$$E = E_0 \exp[i(k_x x \pm k_z z - \omega t)] \quad (2.1.1.1)$$

where  $k_z$  is imaginary and  $k_x$  is real (and the sign of  $k_z z$  term is positive if  $z > 0$ , and negative if  $z < 0$ ). This means that the electric field amplitude decays exponentially in the z-axis and behaves as a propagating wave in the x-axis.

The dispersion relation of surface plasmon polaritons is given by the following equation [11]:

$$k_x = \frac{\omega}{c} \left( \frac{\epsilon_m \epsilon_d}{\epsilon_m + \epsilon_d} \right)^{1/2}$$

(2.1.1.2)

where  $\omega$  is the oscillation frequency,  $\epsilon_m$  is the permittivity of the metal, and  $\epsilon_d$  is the permittivity of the dielectric at the interface. The dispersion relation is demonstrated in Figure 2.1.1.2. Also plotted in the same figure is the dispersion relation of a photon propagating in the adjacent dielectric. Close to the surface plasmon resonance frequency, the wave vector of the surface plasmon polaritons is larger than that of the photon at equal frequencies. This makes it impossible to match the wave vector and the frequency of polaritons and those of the photons at

the same time, which means that surface plasmon polaritons cannot be excited by electromagnetic radiation from the dielectric, and electromagnetic radiation cannot be created in the dielectric by the surface plasmon modes on the metal surface without using additional techniques.

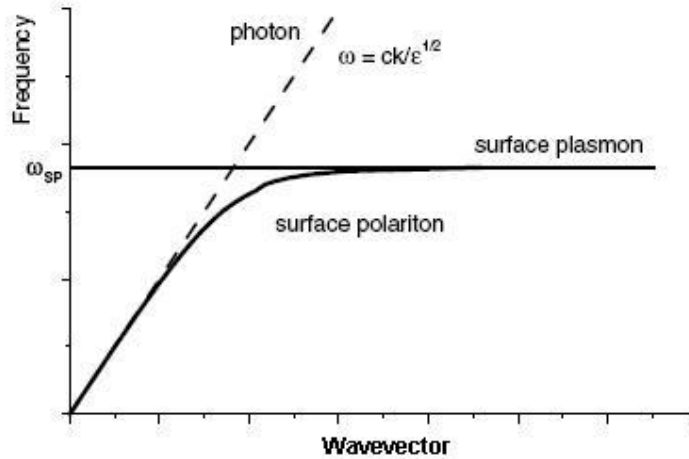
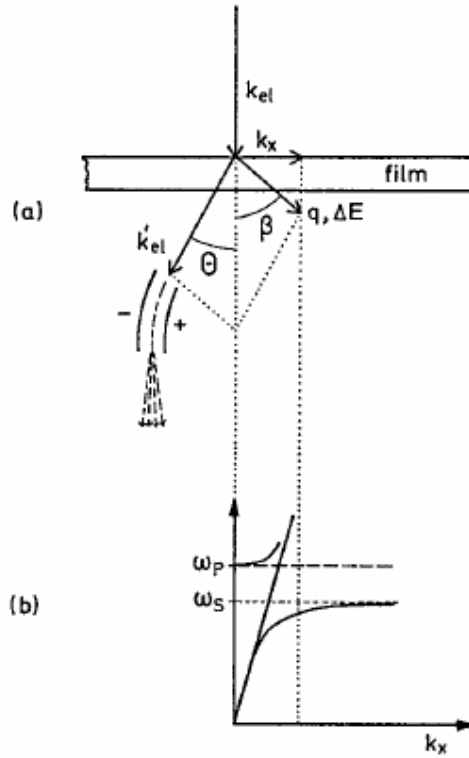


Figure 2.1.1. 2 Comparison of dispersion relations of surface plasmon polariton modes at a metal-dielectric interface and photons in the same dielectric medium (after [12]).

## 2.1.2 Excitation of Surface Plasmon Polaritons

Surface plasmon polaritons can be excited by electrons or by light. Electrons penetrating to the metal surface are scattered and leave some momentum and energy for the electrons on the metal surface. The projection of the momentum on the propagation plane of the surface plasmons determines the wave vector of the excited modes, which is defined as  $k_x$  in the assumption of two dimensions as above. This wave vector also determines the energy through the dispersion relation. Figure 2.1.2.1 presents the scattering of electrons in the metal and displays the position of wave vector on the dispersion curve. The theory of excitation of surface plasmon polaritons by electrons has been verified, finding out the dispersion relation plotted in Figure 2.1.1.2 experimentally [11].



**Figure 2.1.2. 1 Scattering of electrons in the metal film (a), and the position of the corresponding wave vector on the surface on the dispersion curve (after [11]).**

The excitation of surface plasmon polaritons by light requires additional techniques because at a given photon energy the wave vector of surface plasmon polaritons is larger than that of the incident photons as discussed above. One method of achieving this on smooth surfaces is the use of a grating coupler. The light incident on a grating coupler with a grating constant  $a$ , at an angle  $\theta_0$  may have wave vectors  $(\omega/c)\sin\theta_0 \pm vg$  of its component in the surface, where  $v$  is an integer and  $g = 2\pi/a$ . Therefore, the equation

$$k_{SP} = (\omega/c)\sin\theta_0 \pm vg \quad (2.1.2.1)$$

gives the surface plasmon wave vector. The reverse is also valid, in which surface plasmons with the aforementioned wave vectors couple to electromagnetic radiation through a grating coupler.

The second method to excite surface plasmon polaritons on smooth surfaces by light relies on the attenuated total reflection (ATR) coupling. After the reflection of light from a metal surface covered with a dielectric medium with  $\epsilon_0 > 1$ , its momentum is equal to  $(hv/c)\sqrt{\epsilon_0}$  because the speed of light is  $c/\sqrt{\epsilon_0}$  in the dielectric. For an angle of incidence of  $\theta_0$ ,

$$k_x = \frac{\omega}{c} \sqrt{\epsilon_0} \sin \theta_0 \quad (2.1.2.2)$$

is the projection on the surface. Considering the case in Figure 2.1.2.2, the incident light has the wave number projection as in equation 2.1.2.2, and the dispersion relation of surface plasmon polariton modes at the boundary between medium 1 and medium 2 is equal to

$$k_x = \frac{\omega}{c} \left( \frac{\epsilon_m}{\epsilon_m + 1} \right)^{1/2} \quad (2.1.2.3)$$

if medium 2 is air or vacuum. Figure 2.1.2.3 compares the functions in equations 2.1.2.2 and 2.1.2.3, and shows that there is a region of intersection in the graph, which makes it possible to excite surface plasmon modes in the air-metal boundary using total internal reflection from a medium with higher refractive index [11].

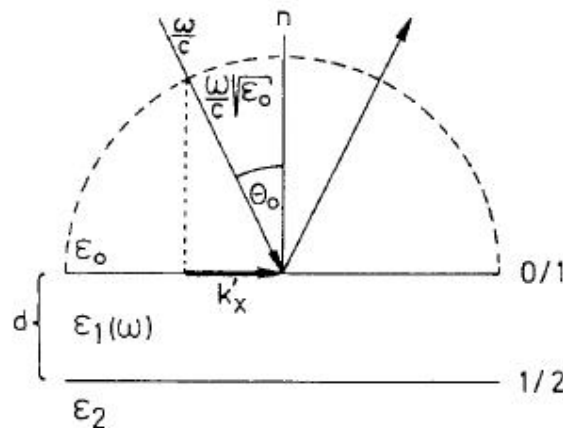


**Figure 2.1.2. 2 Reflection of light at a metal-dielectric boundary. Medium 1 is metal and medium 2 is air or vacuum (after [11]).**

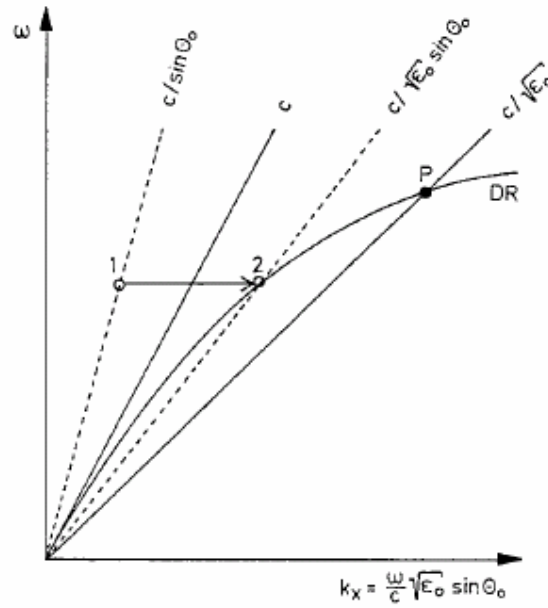


Figure 2.1.2. 3 Comparison of wave vector of light with an angle of incidence of  $\theta_0$  in free space (1) , in medium 0 (2), with the dispersion relation graph of surface plasmon polaritons at medium 1-medium 2 interface (after [11]).

### 2.1.3 Field Enhancement

Since the surface plasmon polariton fields decay perpendicular to the metal-dielectric surface, they are bounded in the near field. Therefore, the field is significantly enhanced at this region. The field enhancement factor at a smooth surface is calculated from

$$\left| \frac{E_{SP}(z=0)}{E_{light}} \right|^2 = \frac{2}{\epsilon_d} \frac{|\text{Re } \epsilon_m|^2}{\text{Im } \epsilon_m} \frac{[\text{Re } \epsilon_m (\epsilon_s - 1) - \epsilon_s]^{1/2}}{1 + |\text{Re } \epsilon_m|} \quad (2.1.3.1)$$

where  $\epsilon_s$  is the permittivity of the prism used to illuminate the metal [12]. The enhancement can be higher than two orders of magnitude for a 60 nm-thick silver film exposed to white light [12].

## 2.2 Localized Surface Plasmons

Localized surface plasmons are the quanta of collective oscillations of electrons spatially confined in metal nanoparticles. Their characteristics are quite different from the surface plasmons on smooth surfaces.

### 2.2.1 Physical Explanation

The response of metal spheres to externally applied electromagnetic radiation can be solved analytically using Maxwell's equations. *Mie* solved this electrodynamic problem completely in 1908 [13]. However, quasi-static approximations also yield reasonably correct results especially for diameters smaller than 30 nm, and they are very helpful to create an intuition on the reader. Therefore, we explain the theory of localized surface plasmon using the quasi-static approximation here.

At optical frequencies, the penetration depth of electromagnetic waves is around 30 nm for gold and silver. As the size of the metal nanoparticle is on the order of penetration depth, the electromagnetic fields can penetrate. This causes electric field formation in the particle. As a result, the conduction band electrons shift collectively with respect to the positive charges in the structure. The collection of the opposite charges at the opposite sides of the particle builds up restoring forces [10]. The restoring forces cause an oscillation of the electrons in the particle. Four factors determine the oscillation frequency: the density and effective mass of the electrons, the shape and size of the charge distribution [14]. The density and effective mass of electrons are material parameters. Metals with high density of electrons have stronger oscillations because of larger polarizability. If the frequency of the exciting electric field is equal to the oscillation frequency of the electrons, even a small excitation brings together very strong oscillations. On the resonance condition, the metal nanoparticle becomes an oscillating dipole, and very high local electric fields are induced in

the incident polarization axis around this dipole [14]. Quasi-static approximation gives the electric field around the metal nanoparticle excited with an E-field polarized in the x-direction with the following equation [14]

$$\bar{E}_{out} = E_0\hat{x} - \alpha E_0 \left[ \frac{\hat{x}}{r^3} - \frac{3x}{r^5}(x\hat{x} + y\hat{y} + z\hat{z}) \right] \quad (2.2.1.1)$$

where  $\alpha$  is the polarizability of the metal particle and  $E_0$  is the amplitude of the incident electric field. The first term on the right hand side is the incident field and the second term on the right hand side is the induced dipole field. From this equation, the induced dipole field has  $1/r^3$  dependence over distance from the center of the particle.

The excited plasmons dampen either in a nonradiative way or by radiating electromagnetic waves. Nonradiative decay is caused by scattering with lattice ions, phonons, the other electrons, surface of the particle, impurities, etc. Nonradiative decay is the dissipation of energy as heat, and contributes to the absorption of the exciting field. Radiative decay occurs as scattering of electromagnetic waves [10]. Both absorption and scattering of the metal nanoparticle are very high around the resonance wavelength, creating a peak at the extinction spectrum. The extinction peak also means local field peak because the electromagnetic field around the particles is linearly proportional to the absorption [15].

Mie theory, neglecting higher order modes, gives the extinction cross section of spherical metal nanoparticles as follows [16]

$$\sigma_{ext} = \frac{9V\epsilon_m^{3/2}}{c} \frac{\omega\epsilon_2(\omega)}{[\epsilon_1(\omega) + 2\epsilon_m]^2 + \epsilon_2(2\omega)^2} \quad (2.2.1.2)$$

where  $V$  is the volume of the particle,  $\omega$  is the frequency of radiation,  $\epsilon_m$  is the dielectric constant of the surrounding medium, and  $\epsilon_{metal} = \epsilon_1 + i\epsilon_2$ . To consider the effect of size differences, size-dependent dielectric constants are used. If  $\epsilon_2$  is small, which is usually the case in our frequency range of interest,

the plasmonic resonance is observed in the extinction cross-section for the case when:

$$\varepsilon_1(\omega) = -2\varepsilon_m \quad (2.2.1.3)$$

This is an important result because it helps us estimate the localized surface plasmon resonance wavelength of metal nanospheres by checking the dispersion relation graphs of the relevant metals. As an example, the dielectric constant of silver as a function of photon energy is displayed in Figure 2.2.1.1 [17]. From this graph, the resonance photon energy for silver nanospheres is expected to be around 3.4 eV.

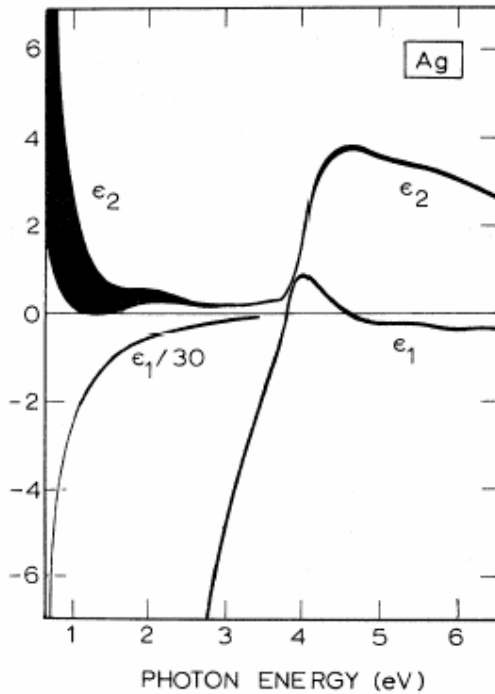


**Figure 2.2.1. 1 Real and imaginary components of the dielectric constant of silver plotted as a function of photon energy. The width of the curves represents the amount of experimental error (after [17]).**

The quasi-static approximation is valid especially for particles with diameters smaller than 30 nm. However, if the diameter of the particle is larger, the quadrupole and octopole modes also become important. In the quadrupole mode, half of the electron cloud moves parallel to the applied field, and the other half

antiparallel to it [14]. For large nanoparticles, a superposition of all modes are observable in the extinction cross section spectrum, and the quasi-static approximation explained above does not yield good enough solutions to the excitation of higher order modes in larger particles, if the size of the particle is comparable to the wavelength of excitation, inhomogeneous polarization becomes valid [16].

## **2.2.2 Parameters Affecting Resonance Conditions**

The type of the metal, the shape and size of the nanoparticle and the environment determine the localized plasmon resonance wavelength together. Let us investigate the effects of all factors on the resonance conditions:

### **2.2.2.1 Size**

The parameters effecting the lifetime of localized plasmon resonance depend on the size. As particle size increases, the effect of radiation damping increases, which causes red-shift and broadening of the plasmon resonance for larger particles [18,19]. The mean free path of electrons in gold is about 50 nm and the electron-phonon collision time is 35 fs. For very small particles collisions with the particle surface become important. Therefore, particle size determines the damping constant [16]. In both extremes, the quality of resonance decreases because the mentioned decay mechanisms become dominant. Therefore, there is an optimum size of metal nanoparticles for better resonance behavior. The proportion of absorption and scattering in the extinction of resonant nanoparticles also depends on the size. As the radiative damping becomes dominant for larger sizes, the scattering is dominant over absorption in larger

nanoparticles [20]. If the particle diameter is greater than 100 nm, extinction is almost 100 % due to scattering [21].

### **2.2.2.2 Shape**

While for small metallic nanospheres only one resonance (the dipole resonance) is valid, for other geometries multiple resonances may be observed. For example, two resonances are observed in triangle structures [22]. For ellipsoids, the resonance wavelength depends on the polarization of the field. If the polarization is in the long axis, the resonance wavelength is longer compared to the polarization in the short axis. The resonance red-shifts if the aspect ratio of the ellipsoid increases. If one dimension of the particle is within 20 nm, the localized plasmon peak shifts to longer wavelengths dramatically [23]. The particle shape has more influence on the resonance wavelength than the size. In the regions of high surface curvature, the enhancement of the local field is higher because of the lightning rod effect [24]. Therefore, nanoparticles with complex shapes including corners yield higher local field enhancement. For example, silver particles in the shape of triangular prisms cause much higher fields than cylinders [23].

### **2.2.2.3 Material**

Metals with higher electron density are better materials for localized plasmon resonance. For this reason, gold and silver are the materials used the most frequently for resonance plasmon resonance applications. The relation given in equation (2.2.1.3) causes the resonance wavelengths of different metals to be different. The dielectric permittivity as a function of wavelength changes from metal to metal and the wavelength at which it satisfies equation (2.2.1.3) also

changes. As an example, for equal particle size and shape and environmental conditions, gold has longer resonance wavelengths than silver.

#### **2.2.2.4 Medium Properties**

Again from equation (2.2.1.3), the dielectric constant of the medium influences the resonance wavelength. The higher the dielectric constant of the medium, the red-shifted the plasmon resonance is. Only the properties of surrounding media close enough to the metal particle can significantly affect the resonance conditions. This distance is around 15 nm. Also, if there are other metal nanoparticles in the environment, the distribution of the electric field, and even resonance wavelength are influenced. Between particles very close to each other, field intensities much higher than those near single particles are observed. However, independent of particle size and shape, for gaps sizes larger than 1 nm, the high intensities rapidly decay. As two particles get close to each other, red-shift is observed in the resonance. The particles can be assumed to be isolated for gap sizes larger than the particle size. If the metal nanoparticles are on metal films, surface plasmon polaritons become an efficient channel for the localized plasmon polaritons to decay, causing significant changes in the resonance conditions [12].

### **2.3 Electromagnetic simulation of localized surface plasmons**

#### **2.3.1 The Finite-Difference Time-Domain Method**

To simulate the response of metal nanoparticles to externally applied electromagnetic radiation, we solve Maxwell's equations using the finite-difference time-domain method. The finite-difference time-domain method

depends on the central difference approximations. Time and space are divided into grids and the derivatives in time and spatial domain are expressed as the changes in the function around a specific grid.

$$\frac{\partial F_{(i,j,k)}^n}{\partial z} = \frac{F_{(i,j,k+1/2)}^n - F_{(i,j,k-1/2)}^n}{\Delta z} + O[(\Delta z)^2] \quad (2.3.1.1)$$

As given in equation 2.3.1.1, the derivative of the function with respect to z is calculated from the difference of the following and previous grid values divided by the grid size. The second term on the right hand side is the second order error term arising from the discretization, and it is ignored in the calculations. The curl equations from Maxwell's equations,

$$\text{Faraday's Law: } \nabla \times \vec{E} = -\vec{\mu} \cdot \frac{\partial \vec{H}}{\partial t} \quad (2.3.1.2-a)$$

$$\text{Ampere's Law: } \nabla \times \vec{H} = \vec{\epsilon} \cdot \frac{\partial \vec{E}}{\partial t} + \vec{J} \quad (2.3.1.2-b)$$

$$\text{Gauss' Law for Electric field: } \nabla \cdot \vec{D} = \rho \quad (2.3.1.2-c)$$

$$\text{Gauss' Law for Magnetic field: } \nabla \cdot \vec{B} = 0 \quad (2.3.1.2-d)$$

are written with all components of the electric and magnetic field vectors, and are discretized using central difference approximations. The electric and magnetic field components are located on a Yee cell as presented in Figure 2.3.1.1.

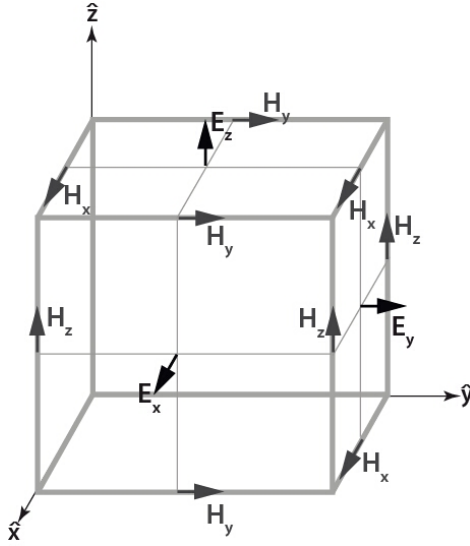


**Figure 2.3.1. 1 Yee cell**

Uniaxial perfectly matched layers (UPML) are used as the boundary conditions. Perfectly matched layers are used to prevent artificial reflection from the boundaries of the computational domain. For more detailed description of the finite-difference time-domain method and uniaxial perfectly matched layers, the reader is suggested to consult [25,26].

## 2.3.2 Implementation

Since metals are involved in our electromagnetic problem, we have to take into consideration the effects of dispersion. Drude model is convenient for silver at optical frequencies, with results compatible with the experimental results. The general equation for Drude model is as follows

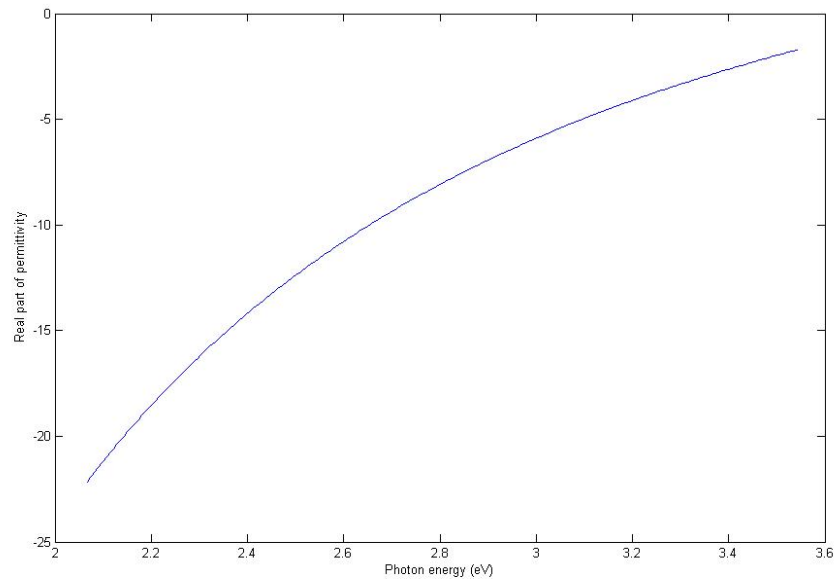
$$\varepsilon_r(\omega) = \varepsilon_\infty - \frac{\omega_p^2}{\omega^2 + j\omega\Gamma} \quad (2.3.2.1)$$

where  $\varepsilon_\infty$  is the dielectric permittivity at infinite frequency,  $\omega_p$  is the plasma frequency and  $\Gamma$  is the relaxation rate of the electrons. For silver, the

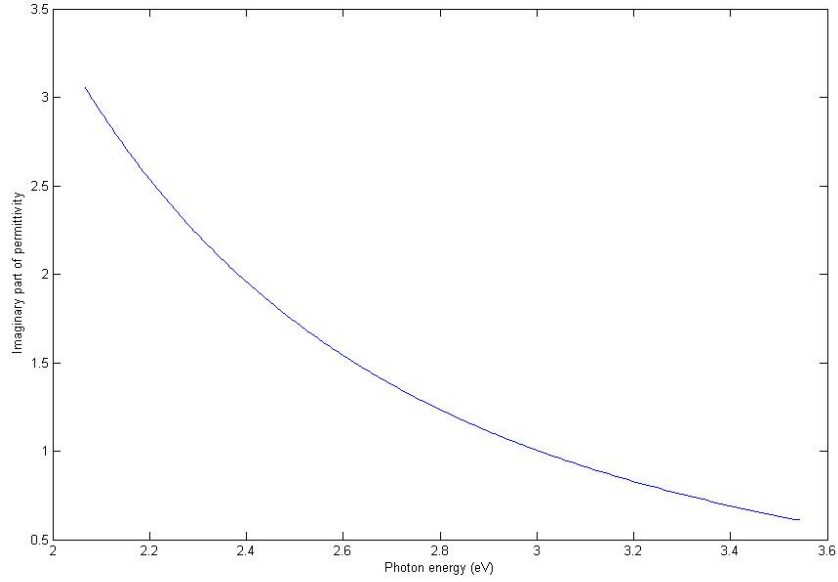
parameters  $\epsilon_\infty = 8.926$ ,  $\omega_p = 11.585$  eV, and  $\Gamma = 0.203$  eV give results similar to the experimental ones in the 350 nm-450 nm range [27]. Figure 2.3.2.1 presents the real and imaginary parts of the dielectric permittivity of silver as a function of photon energy calculated using those parameters in the Drude model. These plots are close to the graph in Figure 2.2.1.1 in our wavelength region of interest.

The wavelength-dependent dielectric constant in the finite-difference time-domain method is introduced in the constitutive relation:

$$\bar{D} = \epsilon_0 \epsilon_r \bar{E} \quad (2.3.2.2)$$



(a)



(b)

**Figure 2.3.2. 1 Real (a) and imaginary (b) parts of the dielectric permittivity of silver plotted using Drude model**

Substituting equation 2.3.2.1 in equation 2.3.2.2 gives the relationship between  $\bar{D}$  and  $\bar{E}$  vectors:

$$\bar{D}(\omega) = \frac{\epsilon_{\infty}\omega^2 + j\omega\epsilon_{\infty}\Gamma - \omega_p^2}{\omega^2 + j\omega\Gamma} \epsilon_0 \bar{E}$$

(2.3.2.3)

Since the finite-difference time-domain method uses time-domain analysis, we have to convert equation 2.3.2.3 from frequency-domain to time-domain. After inverse-Fourier transform is taken,

$$\frac{\partial^2}{\partial t^2} \bar{D} + \Gamma \frac{\partial}{\partial t} \bar{D} = \epsilon_0 \epsilon_{\infty} \frac{\partial^2}{\partial t^2} \bar{E} + \epsilon_0 \epsilon_{\infty} \Gamma \frac{\partial}{\partial t} \bar{E} + \omega_p^2 \epsilon_0 \bar{E} \quad (2.3.2.4)$$

is derived as the differential equation relating  $\bar{D}$  and  $\bar{E}$  vectors. Equation 2.3.2.4 is used in the finite-difference time-domain calculations to include

frequency-dependent dielectric constant of silver. This method is called the “auxiliary differential equation approach” and has been proved to be successful for simulation of dispersive media [28].

The following equations are derived to solve the electromagnetic problems in time domain in the media including dispersive metals, using the auxiliary differential equation approach and uniaxial perfectly matched layers at the boundaries:

$$P_x|_{i+1/2,j,k}^{n+1/2} = \left( \frac{\kappa_y(j) - \sigma_y(j)}{\Delta t} - \frac{\sigma_y(j)}{2\varepsilon_0} \right) P_x|_{i+1/2,j,k}^{n-1/2} + \left( \frac{1}{\frac{\kappa_y(j) - \sigma_y(j)}{\Delta t} + \frac{\sigma_y(j)}{2\varepsilon_0}} \right) \times \left( \frac{H_z|_{i+1/2,j+1/2,k}^n - H_z|_{i+1/2,j-1/2,k}^n}{\Delta y} - \frac{H_y|_{i+1/2,j,k+1/2}^n - H_y|_{i+1/2,j,k-1/2}^n}{\Delta z} \right) \quad (2.3.2.5)$$

$$P_y|_{i,j+1/2,k}^{n+1/2} = \left( \frac{\kappa_z(k) - \sigma_z(k)}{\Delta t} - \frac{\sigma_z(k)}{2\varepsilon_0} \right) P_y|_{i,j+1/2,k}^{n-1/2} + \left( \frac{1}{\frac{\kappa_z(k) - \sigma_z(k)}{\Delta t} + \frac{\sigma_z(k)}{2\varepsilon_0}} \right) \times \left( \frac{H_x|_{i,j+1/2,k+1/2}^n - H_x|_{i,j+1/2,k-1/2}^n}{\Delta z} - \frac{H_z|_{i+1/2,j+1/2,k}^n - H_z|_{i-1/2,j+1/2,k}^n}{\Delta x} \right) \quad (2.3.2.6)$$

$$P_z|_{i,j,k+1/2}^{n+1/2} = \left( \frac{\kappa_x(i) - \sigma_x(i)}{\Delta t} - \frac{\sigma_x(i)}{2\varepsilon_0} \right) P_z|_{i,j,k+1/2}^{n-1/2} + \left( \frac{1}{\frac{\kappa_x(i) - \sigma_x(i)}{\Delta t} + \frac{\sigma_x(i)}{2\varepsilon_0}} \right) \times \left( \frac{H_y|_{i+1/2,j,k+1/2}^n - H_y|_{i-1/2,j,k+1/2}^n}{\Delta x} - \frac{H_x|_{i,j+1/2,k+1/2}^n - H_x|_{i,j-1/2,k+1/2}^n}{\Delta y} \right)$$

(2.3.2.7)

$$D_{x,y,z}|_i^{n+1/2} = \frac{1}{\frac{\varepsilon_\infty}{(\Delta t)^2} + \frac{\varepsilon_\infty \Gamma}{2\Delta t} + \frac{w_p^2}{4}} \times \left[ \begin{aligned} & \left( \frac{2\varepsilon_\infty}{(\Delta t)^2} - \frac{w_p^2}{2} \right) D_{x,y,z}|_i^{n-1/2} - \\ & \left( \frac{\varepsilon_\infty}{(\Delta t)^2} - \frac{\varepsilon_\infty \Gamma}{2\Delta t} + \frac{w_p^2}{4} \right) D_{x,y,z}|_i^{n-3/2} + \\ & \left( \frac{1}{(\Delta t)^2} + \frac{\Gamma}{2\Delta t} \right) P_{x,y,z}|_i^{n+1/2} - \frac{2}{(\Delta t)^2} P_{x,y,z}|_i^{n=1/2} + \\ & \left( \frac{1}{(\Delta t)^2} - \frac{\Gamma}{2\Delta t} \right) P_{x,y,z}|_i^{n=3/2} \end{aligned} \right]$$

(2.3.2.8)

$$E_x|_{i+1/2,j,k}^{n+1/2} = \left( \frac{\kappa_z(k) - \frac{\sigma_z(k)\Delta t}{2\varepsilon_0}}{\kappa_z(k) + \frac{\sigma_z(k)\Delta t}{2\varepsilon_0}} \right) E_x|_{i+1/2,j,k}^{n-1/2} + \left[ \frac{1}{\left( \kappa_z(k) + \frac{\sigma_z(k)\Delta t}{2\varepsilon_0} \right) \varepsilon_0} \right] \times$$

$$\left[ \left( \kappa_x(i) + \frac{\sigma_x(i)\Delta t}{2\varepsilon_0} \right) D_x|_{i+1/2,j,k}^{n+1/2} - \left( \kappa_x(i) - \frac{\sigma_x(i)\Delta t}{2\varepsilon_0} \right) D_x|_{i+1/2,j,k}^{n-1/2} \right]$$

(2.3.2.9)

$$E_y|_{i,j+1/2,k}^{n+1/2} = \left( \frac{\kappa_x(i) - \frac{\sigma_x(i)\Delta t}{2\varepsilon_0}}{\kappa_x(i) + \frac{\sigma_x(i)\Delta t}{2\varepsilon_0}} \right) E_y|_{i,j+1/2,k}^{n-1/2} + \left[ \frac{1}{\left( \kappa_x(i) + \frac{\sigma_x(i)\Delta t}{2\varepsilon_0} \right) \varepsilon_0} \right] \times$$

$$\left[ \left( \kappa_y(j) + \frac{\sigma_y(j)\Delta t}{2\varepsilon_0} \right) D_y|_{i,j+1/2,k}^{n+1/2} - \left( \kappa_y(j) - \frac{\sigma_y(j)\Delta t}{2\varepsilon_0} \right) D_y|_{i,j+1/2,k}^{n-1/2} \right]$$

(2.3.2.10)

$$\begin{aligned}
E_z|_{i,j,k+1/2}^{n+1/2} &= \left( \frac{\kappa_y(j) - \frac{\sigma_y(j)\Delta t}{2\varepsilon_0}}{\kappa_y(j) + \frac{\sigma_y(j)\Delta t}{2\varepsilon_0}} \right) E_z|_{i,j,k+1/2}^{n-1/2} + \left[ \frac{1}{\left( \kappa_y(j) + \frac{\sigma_y(j)\Delta t}{2\varepsilon_0} \right) \varepsilon_0} \right] \times \\
&\left[ \left( \kappa_z(k) + \frac{\sigma_z(k)\Delta t}{2\varepsilon_0} \right) D_z|_{i,j,k+1/2}^{n+1/2} - \left( \kappa_z(k) - \frac{\sigma_z(k)\Delta t}{2\varepsilon_0} \right) D_z|_{i,j,k+1/2}^{n-1/2} \right]
\end{aligned} \tag{2.3.2.11}$$

$$\begin{aligned}
B_x|_{i,j,k}^{n+1/2} &= \frac{2\varepsilon_0\kappa_y(j) - \Delta t\sigma_y(j)}{2\varepsilon_0\kappa_y(j) + \Delta t\sigma_y(j)} B_x|_{i,j,k}^{n-1/2} + \frac{2\varepsilon_0\Delta t}{2\varepsilon_0\kappa_y(j) + \sigma_y(j)\Delta t} \times \\
&\left[ \frac{E_z|_{i,j-1/2,k}^n - E_z|_{i,j+1/2,k}^n}{\Delta y} - \frac{E_y|_{i,j,k-1/2}^n - E_y|_{i,j,k+1/2}^n}{\Delta z} \right]
\end{aligned} \tag{2.3.2.12}$$

$$\begin{aligned}
B_y|_{i,j,k}^{n+1/2} &= \frac{2\varepsilon_0\kappa_z(k) - \Delta t\sigma_z(k)}{2\varepsilon_0\kappa_z(k) + \Delta t\sigma_z(k)} B_y|_{i,j,k}^{n-1/2} + \frac{2\varepsilon_0\Delta t}{2\varepsilon_0\kappa_z(k) + \sigma_z(k)\Delta t} \times \\
&\left[ \frac{E_x|_{i,j,k-1/2}^n - E_x|_{i,j,k+1/2}^n}{\Delta z} - \frac{E_z|_{i-1/2,j,k}^n - E_z|_{i+1/2,j,k}^n}{\Delta x} \right]
\end{aligned} \tag{2.3.2.13}$$

$$\begin{aligned}
B_z|_{i,j,k}^{n+1/2} &= \frac{2\varepsilon_0\kappa_x(i) - \Delta t\sigma_x(i)}{2\varepsilon_0\kappa_x(i) + \Delta t\sigma_x(i)} B_z|_{i,j,k}^{n-1/2} + \frac{2\varepsilon_0\Delta t}{2\varepsilon_0\kappa_x(i) + \sigma_x(i)\Delta t} \times \\
&\left[ \frac{E_y|_{i-1/2,j,k}^n - E_y|_{i+1/2,j,k}^n}{\Delta x} - \frac{E_x|_{i,j-1/2,k}^n - E_x|_{i,j+1/2,k}^n}{\Delta y} \right]
\end{aligned} \tag{2.3.2.14}$$

$$\begin{aligned}
H_x|_{i,j,k}^{n+1/2} &= \frac{2\varepsilon_0\kappa_z(k) - \Delta t\sigma_z(k)}{2\varepsilon_0\kappa_z(k) + \Delta t\sigma_z(k)} H_x|_{i,j,k}^{n-1/2} + \\
&\frac{2\varepsilon_0\kappa_x(i) + \Delta t\sigma_x(i)}{\mu_0\mu_r(2\varepsilon_0\kappa_z(k) + \Delta t\sigma_z(k))} B_x|_{i,j,k}^{n+1/2} + \frac{-2\varepsilon_0\kappa_x(i) + \Delta t\sigma_x(i)}{\mu_0\mu_r(2\varepsilon_0\kappa_z(k) + \Delta t\sigma_z(k))} B_x|_{i,j,k}^{n-1/2}
\end{aligned} \tag{2.3.2.15}$$

$$\begin{aligned}
H_y|_{i,j,k}^{n+1/2} &= \frac{2\varepsilon_0\kappa_x(i) - \Delta t\sigma_x(i)}{2\varepsilon_0\kappa_x(i) + \Delta t\sigma_x(i)} H_y|_{i,j,k}^{n-1/2} + \\
&\frac{2\varepsilon_0\kappa_y(j) + \Delta t\sigma_y(j)}{\mu_0\mu_r(2\varepsilon_0\kappa_x(i) + \Delta t\sigma_x(i))} B_y|_{i,j,k}^{n+1/2} + \frac{-2\varepsilon_0\kappa_y(j) + \Delta t\sigma_y(j)}{\mu_0\mu_r(2\varepsilon_0\kappa_x(i) + \Delta t\sigma_x(i))} B_y|_{i,j,k}^{n=1/2}
\end{aligned} \tag{2.3.2.16}$$

$$\begin{aligned}
H_z|_{i,j,k}^{n+1/2} &= \frac{2\varepsilon_0\kappa_y(j) - \Delta t\sigma_y(j)}{2\varepsilon_0\kappa_y(j) + \Delta t\sigma_y(j)} H_z|_{i,j,k}^{n-1/2} + \\
&\frac{2\varepsilon_0\kappa_z(k) + \Delta t\sigma_z(k)}{\mu_0\mu_r(2\varepsilon_0\kappa_y(j) + \Delta t\sigma_y(j))} B_z|_{i,j,k}^{n+1/2} + \frac{-2\varepsilon_0\kappa_z(k) + \Delta t\sigma_z(k)}{\mu_0\mu_r(2\varepsilon_0\kappa_y(j) + \Delta t\sigma_y(j))} B_z|_{i,j,k}^{n=1/2}
\end{aligned} \tag{2.3.2.17}$$

Equations 2.3.2.5-2.3.2.11 are used to derive the electric field and equations 2.3.2.12-2.3.2.17 are used to derive the magnetic field. These calculations are updated in every time step (and the previous values of the variables are not kept to use the memory efficiently). In the equations, each electric and magnetic field component is written with its location indicated by  $i$ ,  $j$  and  $k$ , and the time step indicated by  $n$ . To make the expressions clear:  $i+1/2$  is  $\Delta x/2$  further from  $i$  in the  $x$ -direction, where  $\Delta x$  is the grid size in the  $x$ -axis. The positions in  $y$  and  $z$  axes are written similarly. In time domain,  $n+1/2$  is  $\Delta/2$  later than  $n$ , where  $\Delta$  is the time grid size.  $\kappa_x$ ,  $\kappa_y$ ,  $\kappa_z$ ,  $\sigma_x$ ,  $\sigma_y$  and  $\sigma_z$  are the UPML parameters. Inside the working region,  $\kappa_x = \kappa_y = \kappa_z = 1$  and  $\sigma_x = \sigma_y = \sigma_z = 0$ . In the UPML region at the boundaries,

$$\kappa_x = 1 + (\kappa_{x\max} - 1) \left( \frac{x}{d} \right)^m \tag{2.3.2.18-a}$$

$$\kappa_y = 1 + (\kappa_{y\max} - 1) \left( \frac{y}{d} \right)^m \tag{2.3.2.18-b}$$

$$\kappa_z = 1 + (\kappa_{z\max} - 1) \left( \frac{z}{d} \right)^m \tag{2.3.2.18-c}$$

where  $d$  is the UPML thickness, the typical values of  $\kappa_{\max}$  are around 7, and  $m$  has a value between 3 and 4.

$$\sigma_x = \sigma_{x \max} \left( \frac{x}{d} \right)^m \quad (2.3.2.19\text{-a})$$

$$\sigma_y = \sigma_{y \max} \left( \frac{y}{d} \right)^m \quad (2.3.2.19\text{-b})$$

$$\sigma_z = \sigma_{z \max} \left( \frac{z}{d} \right)^m \quad (2.3.2.19\text{-c})$$

where

$$\sigma_{x \max} = 1.1 \times \frac{m+1}{150\pi\sqrt{\varepsilon_r}\Delta x} \quad (2.3.2.20\text{-a})$$

$$\sigma_{y \max} = 1.1 \times \frac{m+1}{150\pi\sqrt{\varepsilon_r}\Delta y} \quad (2.3.2.20\text{-b})$$

$$\sigma_{z \max} = 1.1 \times \frac{m+1}{150\pi\sqrt{\varepsilon_r}\Delta z} \quad (2.3.2.20\text{-c})$$

where  $\varepsilon_r$  is the dielectric constant of the medium in the working region.

### 2.3.3 Results

We investigate the electric field distribution around the silver nanoparticle with different excitation types. Both two-dimensional and three-dimensional problems are solved. The silver particle we use in the simulations is a nanosphere in the case of three dimensions, and it is a nanocylinder with infinite height in the case of two dimensions. The simulation area is indicated in the diagram in Figure 2.3.3.1. The excitation is p-polarized from the region shown as the source in the figure. The refractive index of the medium is selected as 1.5

because in most cases the metal nanospheres are dispersed in poly(methyl methacrylate) (PMMA), which has a refractive index of 1.496 [29].

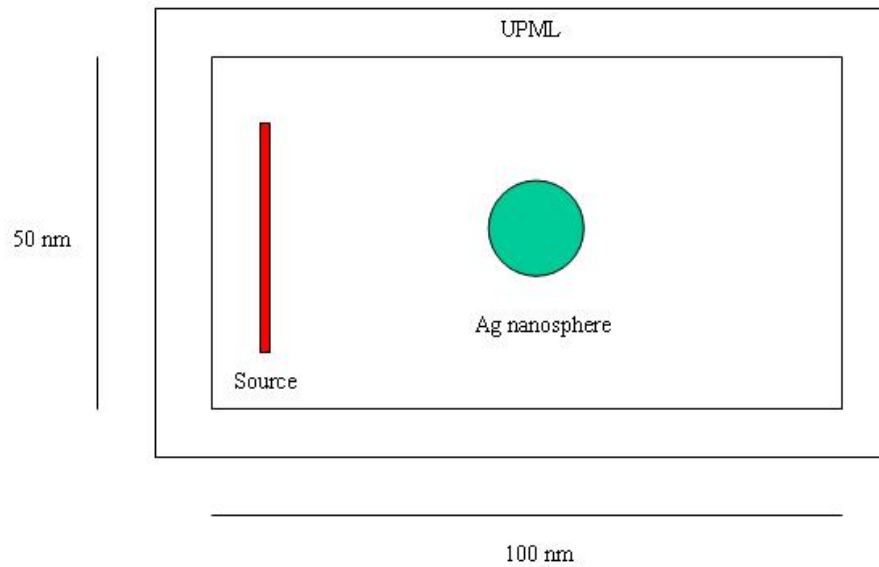


**Figure 2.3.3. 1** Diagram representing the simulation region

Figures 2.3.3.2-2.3.3.4 display the comparison of electric field amplitudes at different distances from the surface of a 10 nm-diameter silver nanocylinder with the electric field at the same locations without the existence of the nanosphere in time domain.

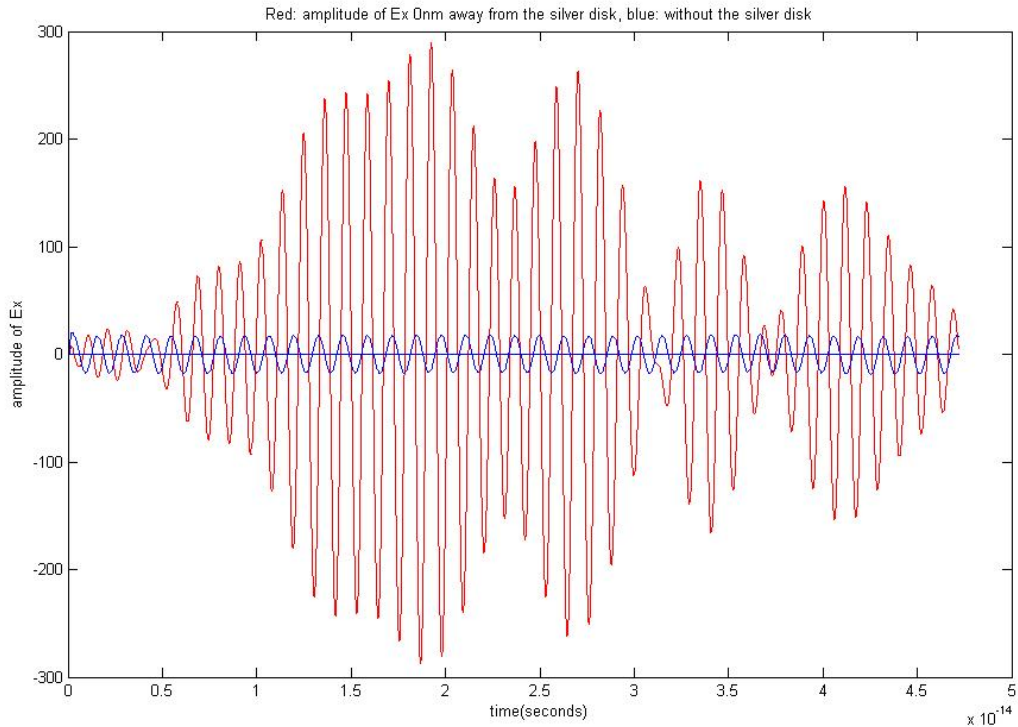


**Figure 2.3.3. 2 The comparison of electric field amplitude at the surface of the nanosphere in longitudinal axis and without the presence of silver nanosphere at the same location when excited at 390 nm free-space wavelength (the unit of x-axis is seconds and the unit of y-axis is arbitrary).**

In Figure 2.3.3.2, the location is at the surface of the nanosphere, whereas the distance to the surface is 0.8 nm in Figure 2.3.3.3 and 1.6 nm in Figure 2.3.3.4. The locations are behind the silver nanosphere (in longitudinal direction) when excited with a continuous wave at 390 nm free-space wavelength. The simulations are undertaken in two dimensions with TE polarization. Figures 2.3.3.5-2.3.3.7 are also the comparisons of the electric field amplitudes at 0 nm, 0.8 nm, and 1.6 nm from the surface of the nanosphere in the transverse axis with respect to the incident wave for the same excitation conditions. These figures prove that large amounts of field enhancement is possible very close to

the surface of the nanosphere, and it decays very rapidly in a few nanometers. Also, the enhanced field at the transverse axis is larger than that in the longitudinal axis.

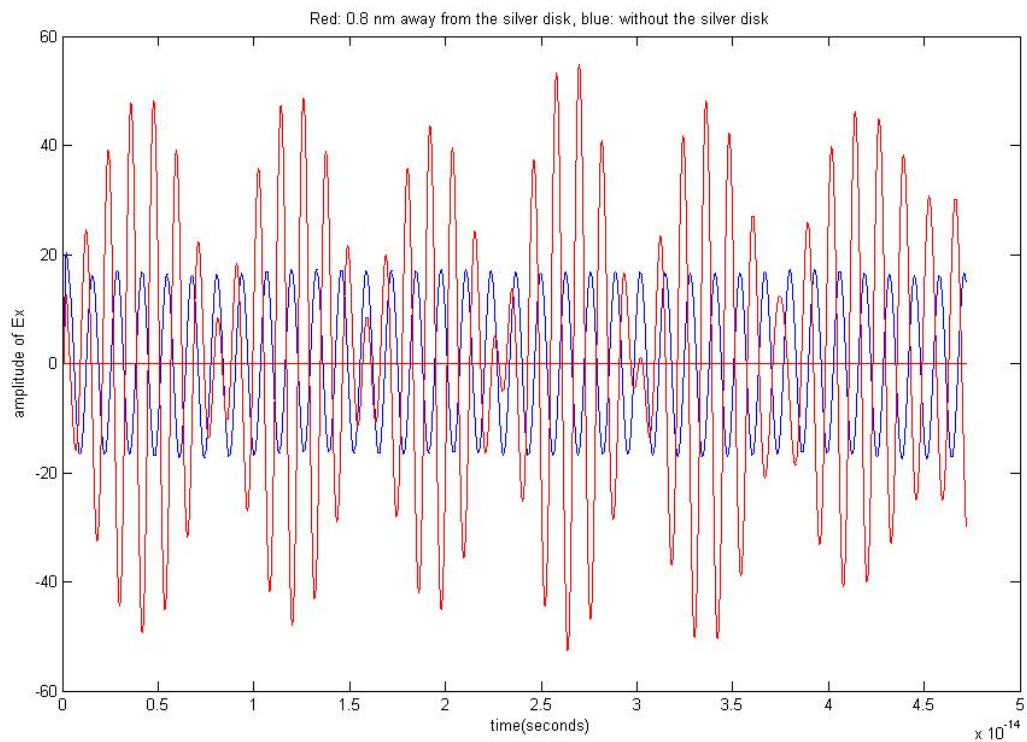


**Figure 2.3.3. 3** The comparison of electric field amplitude at a distance of 0.8 nm from the surface of the silver nanosphere in longitudinal axis and without the silver nanosphere at the same location when excited at 390 nm free-space wavelength (the unit of x-axis is seconds and the unit of y-axis is arbitrary).

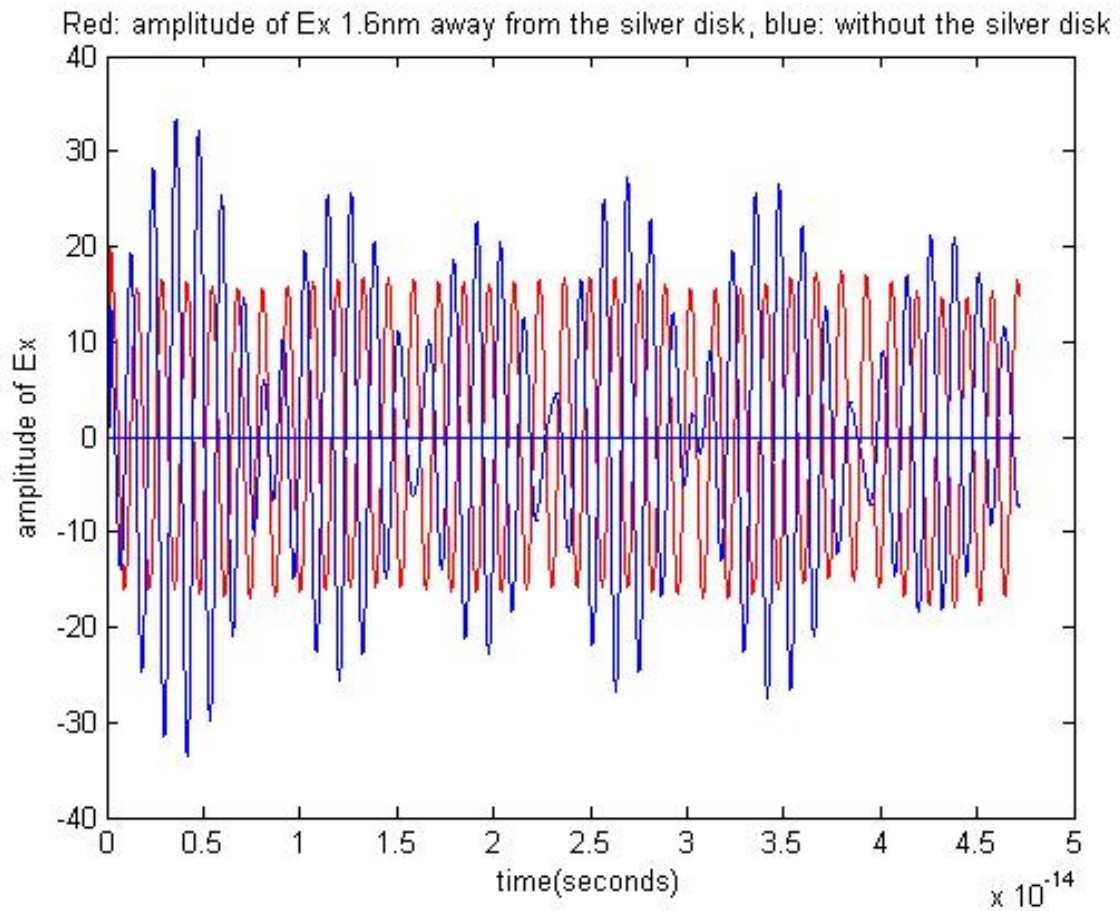


**Figure 2.3.3. 4** The comparison of electric field amplitude at a distance of 1.6 nm from the surface of the silver nanosphere in longitudinal axis and without the silver nanosphere at the same location when excited at 390 nm free-space wavelength (the unit of x-axis is seconds and the unit of y-axis is arbitrary).

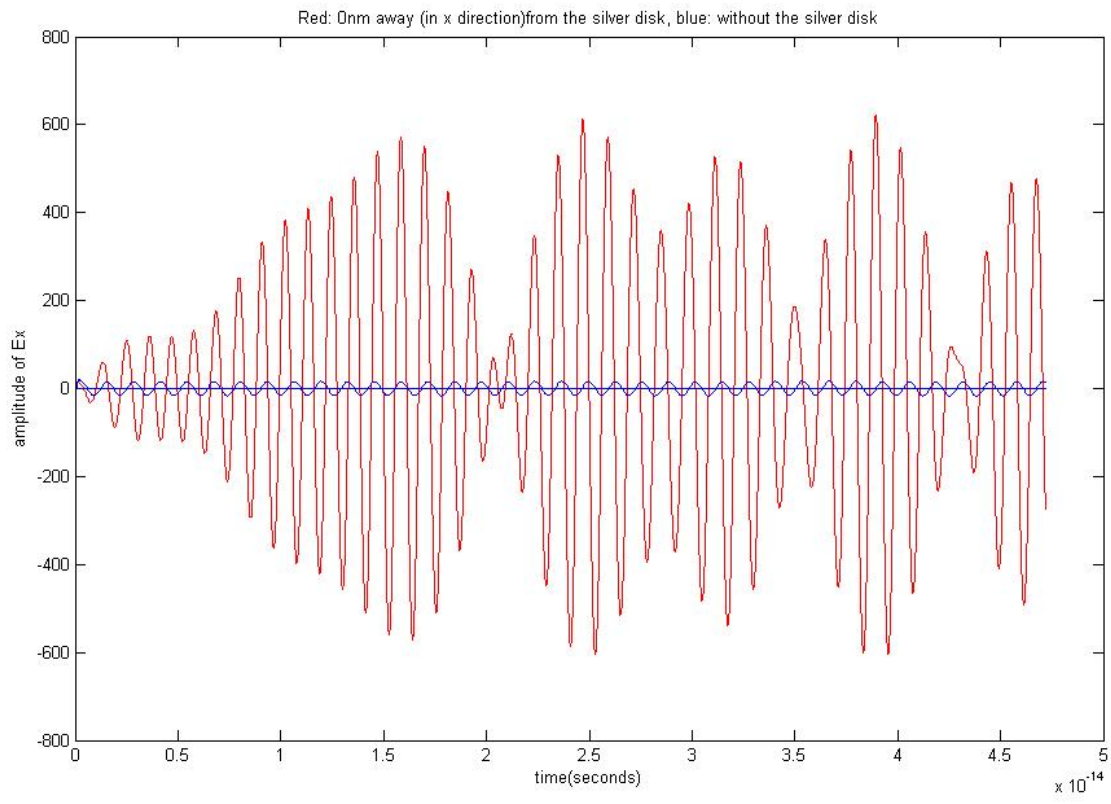


**Figure 2.3.3. 5 The comparison of electric field amplitude at the surface of the silver nanosphere in transverse axis and without the silver nanosphere at the same location when excited at 390 nm free-space wavelength (the unit of x-axis is seconds and the unit of y-axis is arbitrary).**

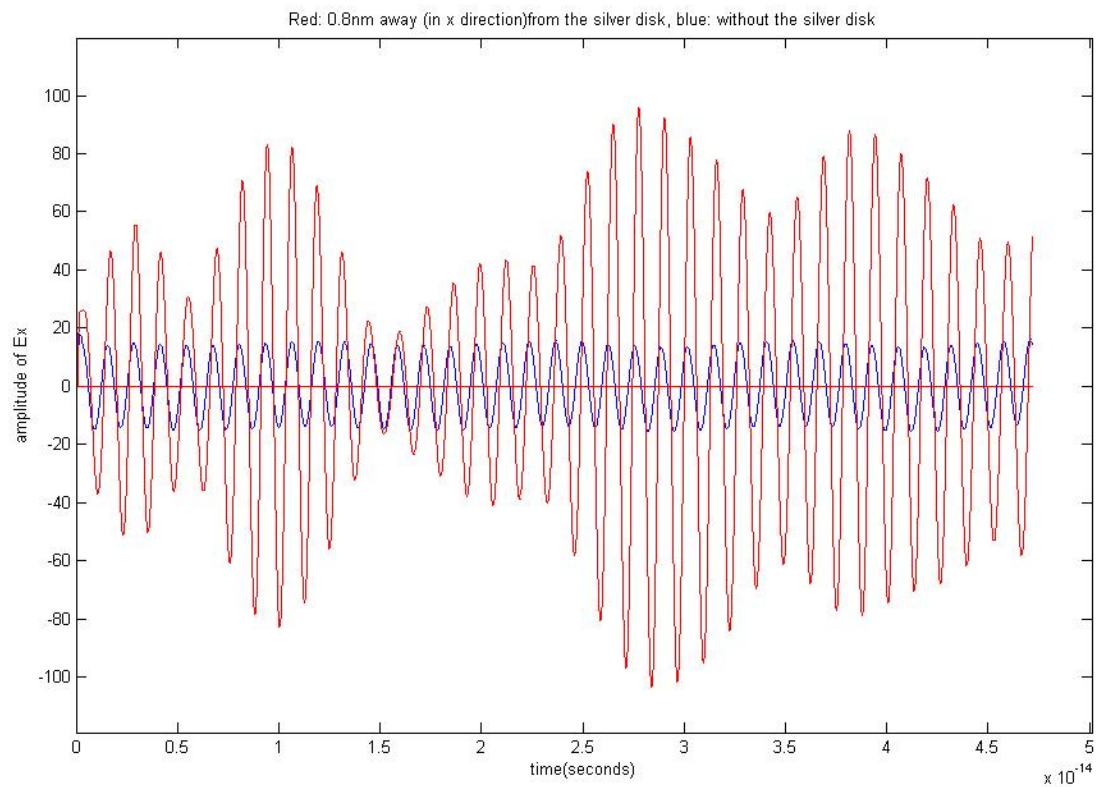


**Figure 2.3.3. 6** The comparison of electric field amplitude at a distance of 0.8 nm from the surface of the silver nanosphere in transverse axis and without the silver nanosphere at the same location when excited at 390 nm free-space wavelength (the unit of x-axis is seconds and the unit of y-axis is arbitrary).

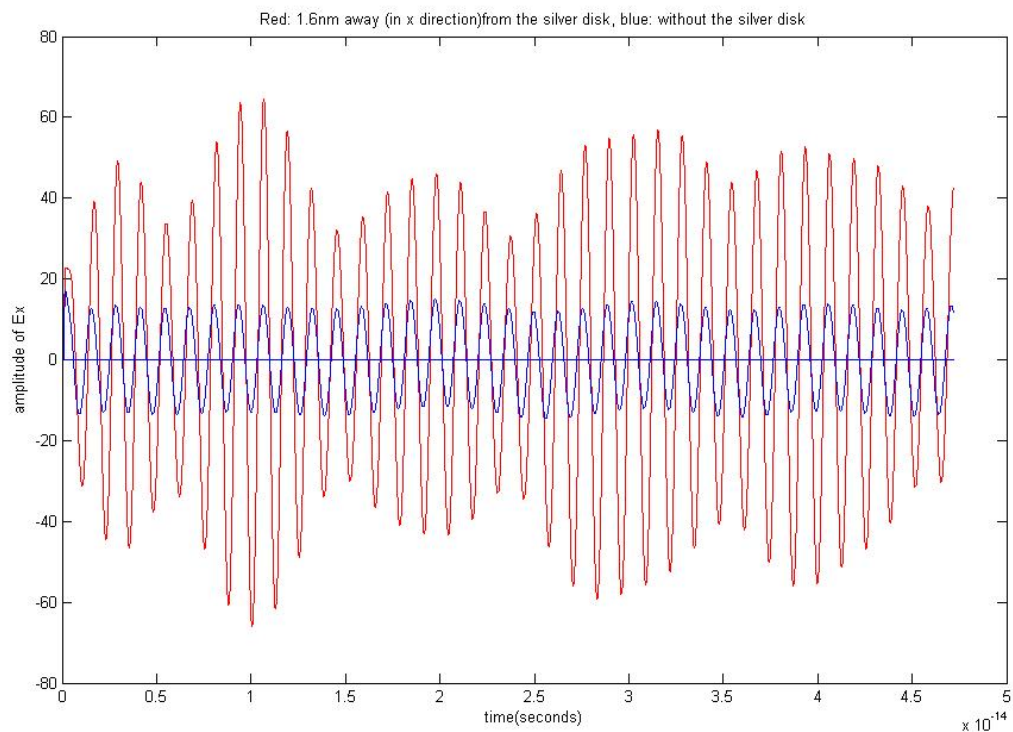


**Figure 2.3.3. 7 The comparison of electric field amplitude at a distance of 1.6 nm from the surface of the silver nanosphere in transverse axis and without the silver nanosphere at the same location when excited at 390 nm free-space wavelength (the unit of x-axis is seconds and the unit of y-axis is arbitrary).**

We also plot the  $1/r^6$  dependence over the distance in Figure 2.3.3.8. This is the expected dependence because the intensity of enhanced electromagnetic field around a metal ellipsoid is proportional to  $1/r^6$  [15], where  $r$  is the distance from the surface.

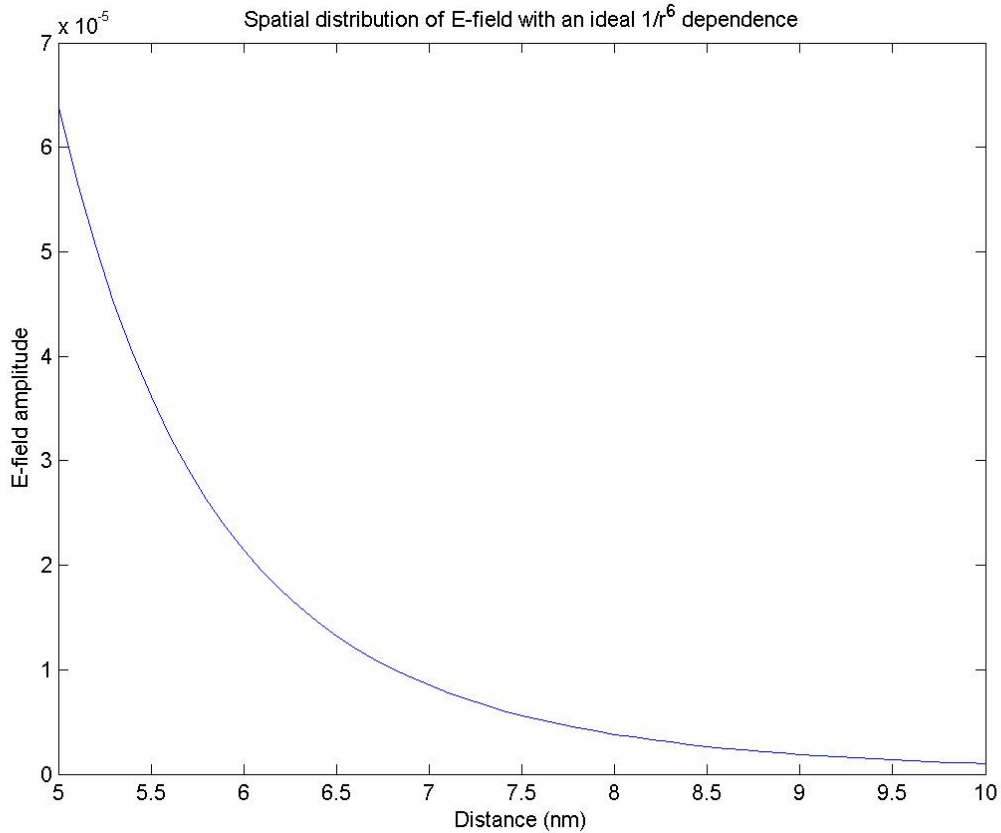


**Figure 2.3.3. 8 Enhanced electromagnetic field intensity distribution with respect to distance from the surface with a  $1/r^6$ -dependence (the unit of x-axis is nm and the unit of y-axis is arbitrary).**

Additionally, we excite the nanocylinder with a beam, which is Gaussian in time in order to investigate the spectral response. The full-width at half-maximum of the beam is 50 fs. The medium is considered as free space. We make simulations with and without the silver nanocylinder and take the Fourier transform of the electric field amplitude in both cases. Figure 2.3.3.9 plots the spectral distribution of the electric field amplitude at the surface of the silver nanocylinder with a 10 nm diameter. The resonance around 340 nm free-space wavelength is clearly visible. This resonance wavelength is slightly shorter than the reported value in the literature, which is 370 nm [22]. The possible reason might be the different Drude model parameters used for silver. However, this

graph proves that a local field enhancement is observed around the resonance wavelength of silver nanoparticles.

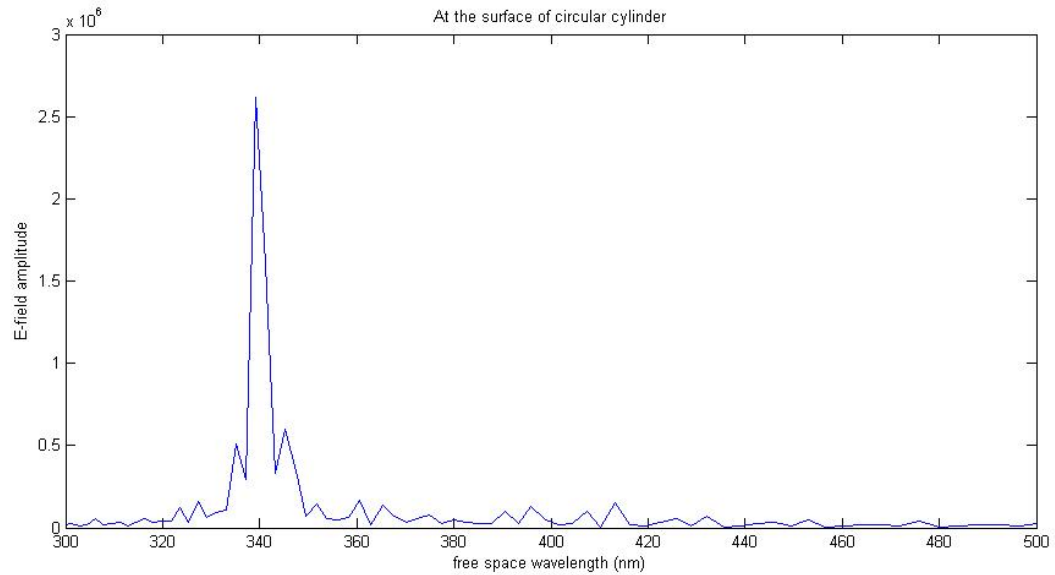


**Figure 2.3.3. 9 Spectral distribution of electric field amplitude at the surface of silver nanocylinder (the unit of x-axis is nm and the unit of y-axis is arbitrary).**

# Chapter 3

## Semiconductor Nanocrystals

### 3.1 Theory

#### 3.1.1 Definition and Basics

Nanocrystals are aggregates of a few hundred to tens of thousands of atoms that combine into a crystalline form of matter known as a cluster. The size of these crystallites ranges from one to tens of nanometers. Within this range of sizes, nanocrystals are larger than molecules, but still much smaller than bulk materials. What makes nanocrystals different from other quantum-confined structures, i.e., quantum wells and quantum wires is the fact that quantum wells and quantum wires have translational symmetry in one or two dimensions, but in nanocrystals translational symmetry is totally broken because there are only a finite number of electrons and holes within the same crystal. As a result, the concepts of electron-hole gas and quasi-momentum cannot be applied to nanocrystals. Also, the finite number of electrons in nanocrystals causes a variety of photoinduced phenomena such as persistent and permanent photophysical and photochemical phenomena, which are known in atomic and molecular physics, but are not applicable to solids. Another point which makes nanocrystals different is their fabrication techniques. Nanocrystals are fabricated using techniques also used in glass technology and colloidal chemistry [30].

### 3.1.2 Energy States in Quantum Dots

In theoretical analysis, nanocrystals are assumed to be a tiny piece of a crystal structure with a spherical or cubic shape, which is known as a quantum dot. In fact, such perfectly spherical or cubic species do not exist in reality. However, this assumption is very useful to understand the physics of nanocrystals by using simplified models and the basic effects coming from three-dimensional spatial confinement. Therefore, particle-in-a-box problem is solved for a simple analysis here. At smaller sizes, quantum chemical approach is used, in which the number of atoms is taken into account instead of the size.

Effective mass approximation is used in the analysis of nanocrystals. According to this approximation, electrons (and holes) are assumed to have the same effective mass as in the ideal infinite crystal of the same stoichiometry. In this approach, we treat the crystallite as a macroscopic crystal with respect to the lattice properties, but consider it as a quantum dot for quasiparticles. The simplest model to analyze nanocrystals is the spherical potential box with infinite potential barriers and with electrons and holes considered to have isotropic effective masses. This problem can be investigated for two different cases of the weak confinement regime and the strong confinement regime.

The weak confinement regime is considered when the dot radius  $a$  is small, but still a few times larger than the exciton Bohr radius,  $a_B$ . To give an idea, the exciton Bohr radius is 4.9 nm for CdSe, 2.8 nm for CdS, and 3.8 nm for ZnSe [31]. The exciton center-of-mass motion has quantization in this case. The dispersion law of an exciton in a crystal is as follows:

$$E_n(K) = E_g - \frac{R_y^*}{n^2} + \frac{\hbar^2 K^2}{2M} \quad (3.1.2.1)$$

where  $K$  is the magnitude of the exciton wave vector,  $E_g$  is the bandgap energy of the crystal structure,  $R_y$  is the exciton Rydberg energy,  $n$  are quantum

numbers, and  $M$  is the exciton mass calculated from the effective electron mass and the effective hole mass as in equation 3.1.2.2.

$$M = m_e^* + m_h^* \quad (3.1.2.2)$$

In equation 3.1.2.1, the second term on the right hand side represents the Coulomb interaction between the electron and the hole, and the third term comes from the kinetic energy of the exciton. For the case of a nanocrystal, the kinetic energy term in this equation has to be modified because the kinetic energy of an exciton in a quantum dot is discrete. The discrete values can be calculated by solving the particle in a spherical box problem. With the change in the kinetic energy term, equation 3.1.2.1 becomes:

$$E_{nml} = E_g - \frac{R_y^*}{n^2} + \frac{\hbar^2 \chi_{ml}^2}{2Ma^2} \quad (3.1.2.3)$$

where  $a$  is the quantum dot radius,  $\chi_{ml}$  are the roots of the Bessel function coming from the center-of-mass motion in a spherical box with infinite external potential barriers.  $l$  is the orbital number, determining the angular momentum, and  $m$  is the magnetic number, which determines the angular momentum component parallel to the  $z$  axis. Since photon absorption can create excitons with zero angular momentum only, the absorption spectrum is derived from the equation above, but with the case that  $l$  is equal to zero:

$$E_{nm} = E_g - \frac{R_y^*}{n^2} + \frac{\hbar^2 \pi^2}{2Ma^2} m^2 \quad (3.1.2.4)$$

Equation 3.1.2.4 describes the energy levels for optical transitions in the weak confinement regime [30].

In the strong confinement regime, the dot radius  $a$  is much smaller than the exciton Bohr radius,  $a_B$ . If we assume that the confined electron and hole are both free and model the nanocrystal as a spherical box in an infinite potential wall [32]:

$$E_{ml}^e = E_g + \frac{\hbar^2 \chi_{ml}^2}{2m_e a^2} \quad (3.1.2.5)$$

$$E_{ml}^h = \frac{\hbar^2 \chi_{ml}^2}{2m_h a^2} \quad (3.1.2.6)$$

Under this assumption, the term representing the Coulomb interaction disappears because the electron and hole are assumed to be free in this case. Of course this is not correct and we need to come back to this to correct for the strong Coulomb interaction. From equations 3.1.2.5 and 3.1.2.6, we can find the energy difference between the lowest electron and hole 1s states. For this condition,  $l=0$ , and  $m=1$ . The energy difference is then

$$E_{1s1s} = E_{1s}^e + E_{1s}^h = E_g + \frac{\hbar^2 \pi^2}{2a^2} \left( \frac{1}{m_e} + \frac{1}{m_h} \right) \quad (3.1.2.7)$$

This is the minimal energy required to create an unbound electron-hole pair. Optical transitions require the electron and hole states to have the same principal and orbital quantum numbers. As a result, the absorption spectrum reduces to a set of discrete bands with peaks at the energies:

$$E_{nl} = E_g + \frac{\hbar^2}{2\mu a^2} \chi_{nl}^2 \quad (3.1.2.8)$$

where

$$\frac{1}{\mu} = \frac{1}{m_e} + \frac{1}{m_h} \quad (3.1.2.9)$$

Because of this absorption spectrum with discrete peaks, quantum dots in the strong confinement limit are referred to as artificial atoms [30].

This model, which ignores the Coulomb interactions because of the absence of a hydrogen atom-like exciton behavior, is not correct because the electron and hole are confined in space comparable to the extension of the exciton ground

state in the ideal crystal. On the contrary, the Coulomb interaction between the electron and the hole is even stronger in the strong confinement limit of quantum dots. Therefore, the energy difference between the lowest electron and hole states is corrected as

$$E_{1s1s} = E_g + \frac{\hbar^2 \pi^2}{2\mu a^2} - 1.786 \frac{e^2}{\epsilon a}$$

(3.1.2.10)

with the addition of the last term representing Coulomb interaction [33]. This phenomenon is referred to as “exciton in quantum dot”.

We arrive at a very important conclusion from both equations 3.1.2.7 and 3.1.2.10, independent of the assumptions used in the calculations. Both equations express that the optical transition energy edge significantly depends on the radius of the quantum dot. This is one of the most important characteristics of semiconductor nanocrystals, making it possible to engineer their optical absorption edge and emission peak wavelengths by controlling the size during synthesis.

### 3.1.3 Broadening mechanisms

Both homogeneous and inhomogeneous broadening are effective in the optical characteristics of semiconductor nanocrystals. Homogeneous broadening is observed even in single nanocrystals because of dephasing, which occurs through events such as radiative recombination or scattering of the electron-hole pair with impurities, phonons, or imperfections in the structure.

The other broadening mechanism in semiconductor nanocrystals is inhomogeneous broadening. This occurs in nanocrystal ensembles because of the size distribution. Except some specific cases, where all the nanocrystals have exactly equal number of atoms, nanocrystals with slightly different sizes co-exist. We can take into account the effect of inhomogeneous broadening on the

absorption spectrum by multiplying the absorption coefficient of every single size with the probability of the existence of that size, and adding all the terms as follows:

$$\alpha(\omega)_{av} = \int P(R)\alpha(\omega)_R dR \quad (3.1.3.1)$$

In most cases, Gaussian distribution is valid for the probability distribution of the quantum dot radii in an ensemble with enough number of nanocrystals.

The effect of both homogeneous and inhomogeneous broadening on the absorption and emission spectra is significant. As indicated in Section 3.1.2, optical transitions in strongly-confined nanocrystals occur at well-separated energy levels. However, broadening mechanisms cause those well-separated absorption peaks to combine into a single absorption curve in the spectrum. A crystal size distribution of 10 % is enough to transform the discrete absorption spectrum into a continuous one. This evolution is clearly shown in Figure 3.1.3.1, where the absorption spectrum of a semiconductor nanocrystal is plotted with size distributions from 5% to 20%.

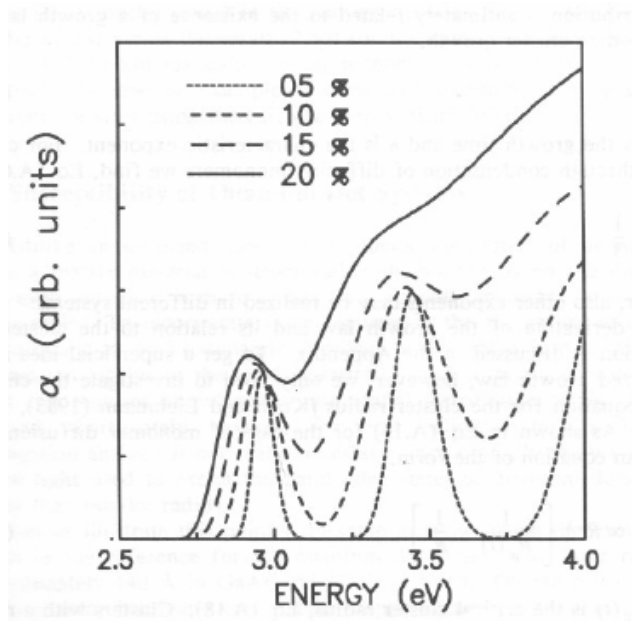


**Figure 3.1.3. 1 Evolution of the optical absorption spectrum of semiconductor nanocrystals with full-width at half-maximum enlarging with increasing size distribution in the ensemble (after [32]).**

## **3.2 Experimental Characterization**

It is possible to make experiments with semiconductor nanocrystals under different conditions, which gives freedom of choice to some extent. While nanocrystals can be kept in polymer matrices, they can also be kept as colloids in materials such as chloroform or toluene and they can be used without any other host materials in the environment. We have experience on all such techniques of handling nanocrystals.

### **3.2.1 Nanocrystal Processing Techniques**

It is helpful to summarize some nanocrystal processing techniques at this point. For some applications the nanocrystals have to be cast in thin films with well-controlled thicknesses. Embedding them in polymer matrices is one solution. Poly(methyl methacrylate) (PMMA) is a polymer that conveniently forms uniform films with spin-coating technique. Nanocrystals can be dispersed quite uniformly in PMMA matrix. The nanocrystals can be dispersed also in different polymers with different levels of viscosities, leading to different thicknesses after spin-coating. For instance, by spin-coating at a speed of 3000 revolutions per minute (rpm), it is possible to obtain polymer films of varying viscosity with thicknesses ranging from 10 nm to 2  $\mu\text{m}$ . In polymer matrix, the nanocrystals are isolated from each other unless the nanocrystal concentration is very high. Another type of host medium for semiconductor nanocrystals is solvents such as chloroform, toluene and acetone. It is difficult to obtain controlled film thicknesses with this kind of matrices. They are good for applications including colloidal suspensions of mobilized nanocrystals.

If closely-packed nanocrystals are required, the colloidal suspensions mentioned above can be further processed. One method is to disperse them in chloroform, which evaporates rapidly, and then to drop-cast or dip-coat to form a thin film of nanocrystals. During the evaporation process, the nanocrystals in a

droplet of solvent located on the substrate are kept in an environment with controlled air flow and pressure. As a result of this process, the chloroform is evaporated and closely-packed nanocrystals are left on the substrate.

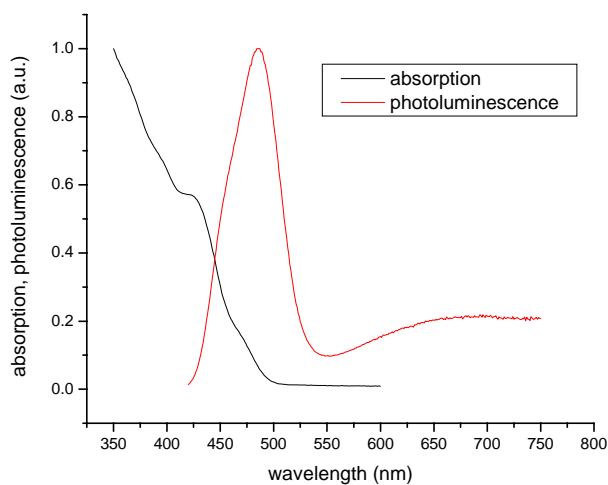
The efficiency of each technique depends on the properties of the nanocrystals. If the nanocrystals do not have shells or other additional materials covering them, they form aggregations and start behaving like bulk materials if they are kept very close to each other. They have to be suspended in low concentration in a host medium. However, in some applications the nanocrystals have to be in closely-packed form. For those cases, nanocrystal surfaces have to be modified to avoid aggregation or bulk material formation. Trioctylphosphine oxide (TOPO) is a common surfactant used to coat the outer layer of nanocrystals to prevent aggregation. In hot injection method, the nanocrystals end up with TOPO coating on their outmost shells as a result of the natural synthesis process starting with organic based sources.

Before processing nanocrystals for device fabrication or experimental characterization, it is useful to clean the colloidal material from undesired organic contaminants. This can be achieved by adding methanol or acetone at equal volume and then centrifuging with speeds higher than 5000 rpm. This way, nanocrystals are separated from the other materials including the contaminants. Repeating the centrifuge more than twice separates the organic contaminants almost completely. It is commonly suggested to repeat this purifying process at least three times.

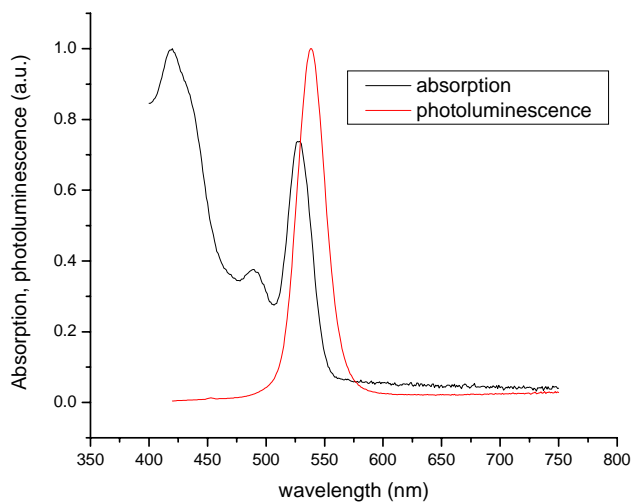
### **3.2.2 Optical Absorption and Emission Measurements**

As mentioned in Section 3.1, the optical absorption and emission spectra of semiconductor nanocrystals are strongly dependent on the size distribution of the quantum dots because the discrete energy levels significantly alter with

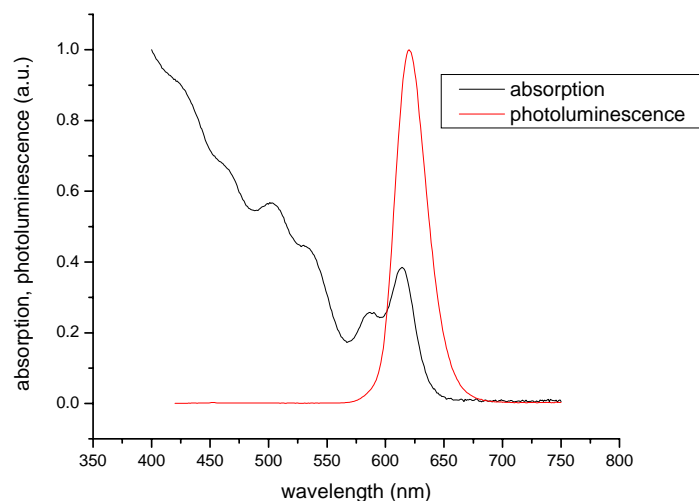
changing radii of the quantum dots. As expressed in equation 3.1.2.10, the energy difference between the 1s states of the electrons and holes increases with decreasing size. Therefore, the peak emission wavelength and optical absorption edge wavelength are blue-shifted with decreasing size. Figures 3.2.2.1(a,b,c) display the absorption and photoluminescence spectra of some CdSe/ZnS core-shell nanocrystals together.



(a)



(b)



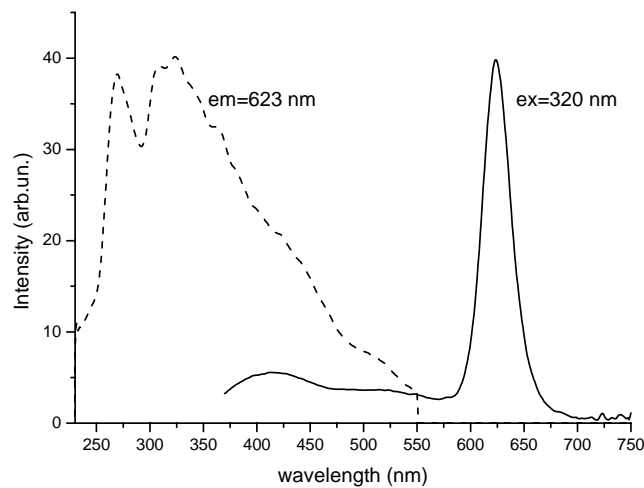
(c)

**Figure 3.2.2. 1 Absorption and photoluminescence spectra of CdSe/ZnS core-shell nanocrystals with diameters of 2.1 nm (a), 2.7 nm (b), and 5.3 nm (c).**

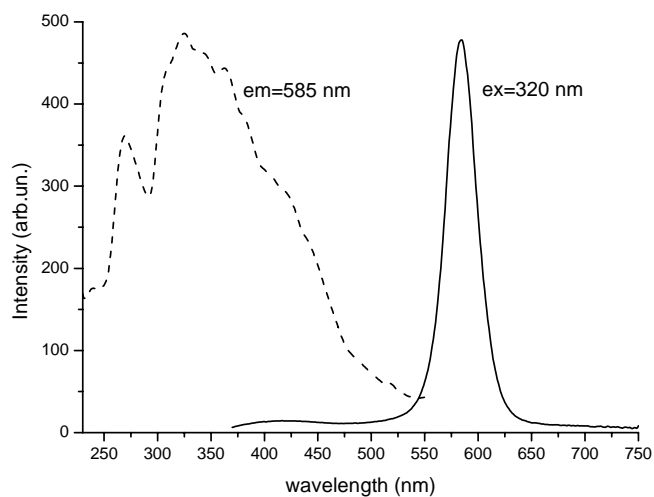
The emission wavelength is red-shifted with respect to the absorption edge because of the energy losses occurring through different mechanisms when the nanocrystals are in the excited state. This phenomenon is called “Stokes shift”. The exciton peak is also visible in the absorption spectrum, close to the absorption edge.

Figure 3.2.2.2 shows the photoluminescence excitation (PLE) spectra of CdSe/ZnS nanocrystals with the photoluminescence spectra on the same graph. The excitation spectrum of the nanocrystals is measured by exciting the materials with a light source and a monochromator so that the excitation wavelength can be tuned. The emitted light intensity is measured at the peak emission wavelength and normalized with respect to the intensity of the corresponding excitation wavelength. The excitation spectra show that the absorption increases in shorter wavelengths, which causes more electron-hole pairs to form and more photons to be emitted, as expected. The decrease of the PLE in deep ultraviolet is not related to the CdSe/ZnS nanocrystals, but it is because of the polymer, which is the host material used in these samples. The

absorption of the polymer becomes dominant for wavelengths shorter than 300 nm, and prevents the nanocrystals from being excited, thus decreasing the emission intensity.



(a)

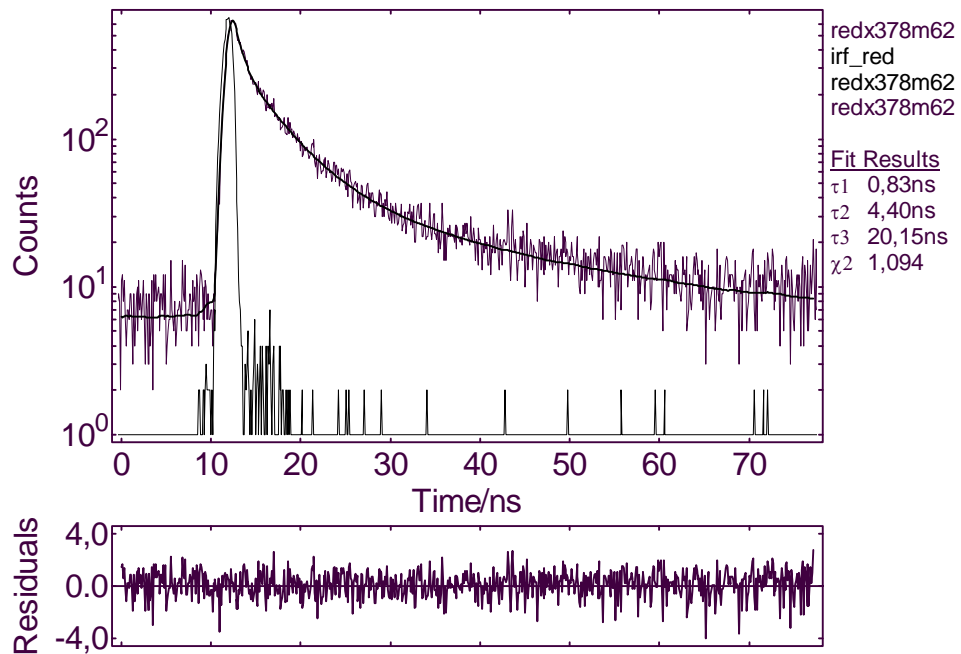


(b)

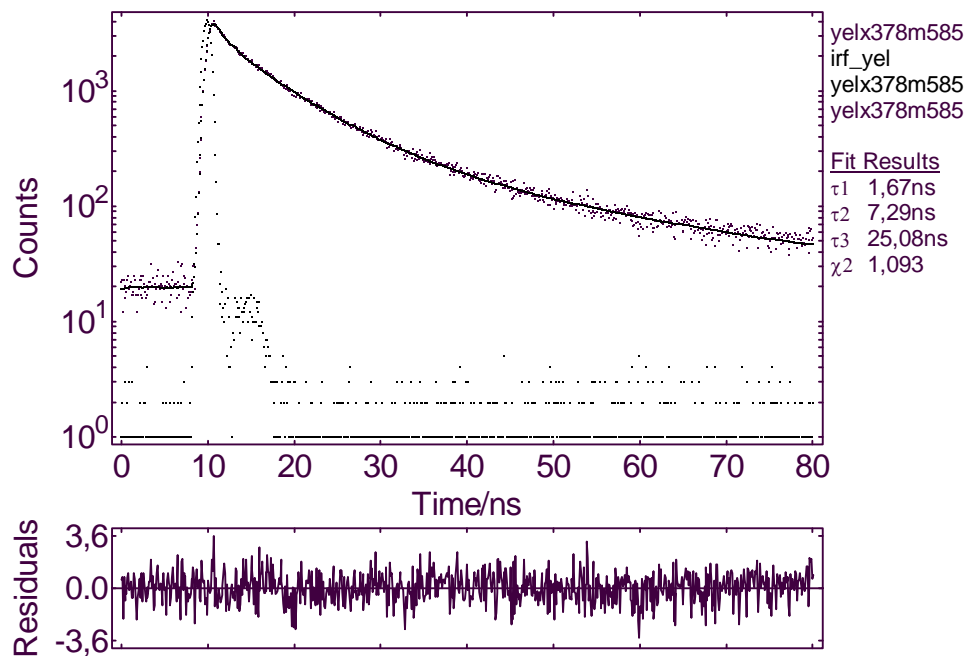
**Figure 3.2.2. 2 Photoluminescence excitation and photoluminescence spectra of CdSe/ZnS nanocrystals with peak emission wavelength of 623 nm (a) and 585 nm (b).**

We also make time-resolved emission measurements of the nanocrystals. Time-resolved emission measurement is taken by exciting the material with a pulse short enough such that the decay of the emission (i.e., lifetime of the emission) can be observed. In our measurement, the excitation wavelength is 378 nm. Figure 3.2.2.3 presents the number of photons collected from two different CdSe/ZnS nanocrystals in time after excitation. The lifetimes are in the order of a few nanometers. The lifetime of light-emitting materials are important for applications with speed and bandwidth requirements.

Both the photoluminescence excitation and time-resolved photoluminescence measurements have been completed at the Institute of Molecular and Atomic Physics of Belarus with our participation as a collaborative research effort within European Union FP6 Network of Excellence: PhOREMOST (Nanophotonics to Realize Molecular Scale Technologies).



(a)



(b)

**Figure 3.2.2. 3 Time-resolved photoluminescence of CdSe/Zns core-shell nanocrystals with emission wavelengths of 585 nm (a) and 620 nm (b).**

### 3.2.3 Electromodulation of Optical Properties of CdSe Nanorod and Nanodot Films

Optoelectronic nanodevices that rely on the electric field effects in optical absorption and emission provide the ability to be externally controlled conveniently using integrated electronic platforms. As an excellent candidate for such optoelectronic nanomaterials semiconductor quantum dots are theoretically expected to show strong electric field dependent optical properties [30]. In the general class of quantum dots, chemically synthesized semiconductor nanocrystals also exhibit electric field effects, for example, as demonstrated in their optical absorption (e.g. through quantum confined Stark effect [34, 35]) and in their optical emission as Stark shift and luminescence quenching [36]).

We investigate the influence of external electric field on the photoluminescence and optical absorption properties of chemically synthesized CdSe nanorods and nanodots. Unlike quantum dots, the nanorods exhibit quantum confinement only in two dimensions. It is suggested that the electric field applied along the nanorods length may provide effective exciton dissociation resulting in the strong photoluminescence quenching (especially if the nanorods were aligned).

For the electromodulation experiments with the nanorods and nanodots, we prepare the sample by placing the polymeric PMMA film with CdSe nanorods or nanodots between two transparent indium tin oxide (ITO) electrodes sealed with epoxy glue. The electric field influence on the photoluminescence of the nanocrystal is studied by applying constant voltages between transparent ITO electrodes. The PL is excited by 488 nm Ar-ion laser. The PL spectra at different voltages are measured by combination of inverted microscope and LN-cooled CCD camera based spectrometer. In Figure 3.2.3.1, we present the photoluminescence spectra of CdSe nanorods at different applied voltages.

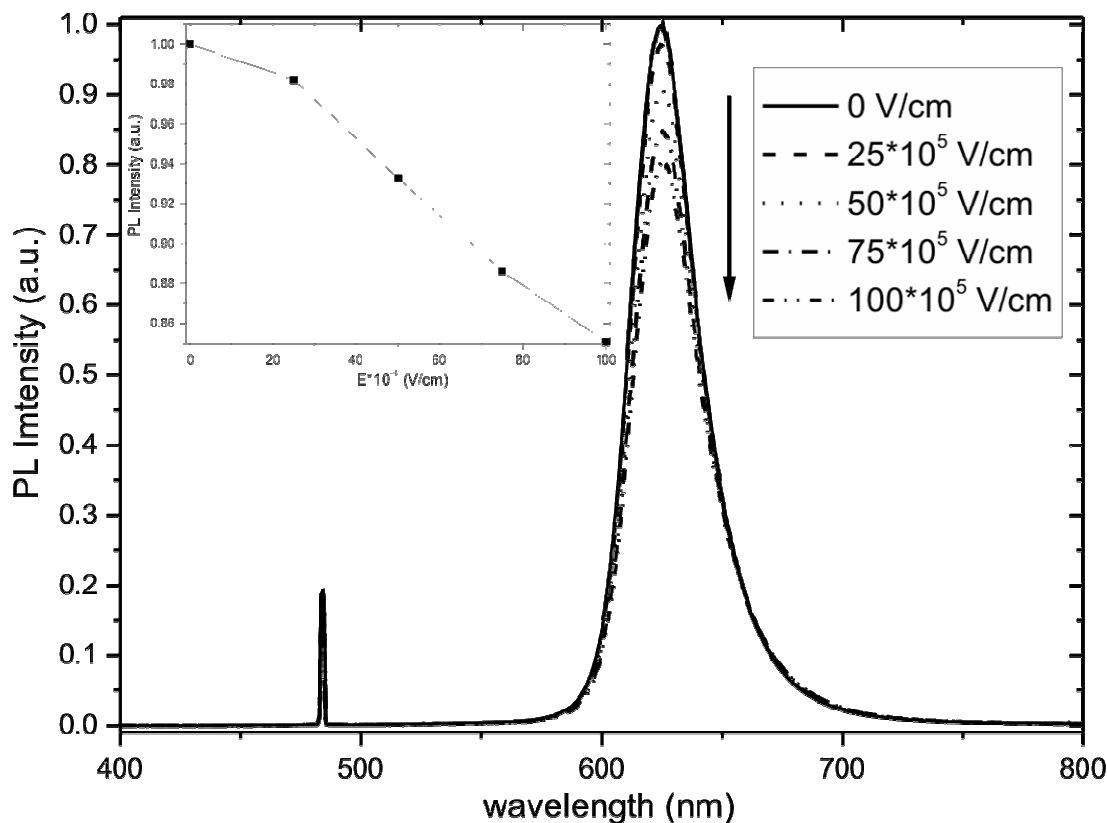
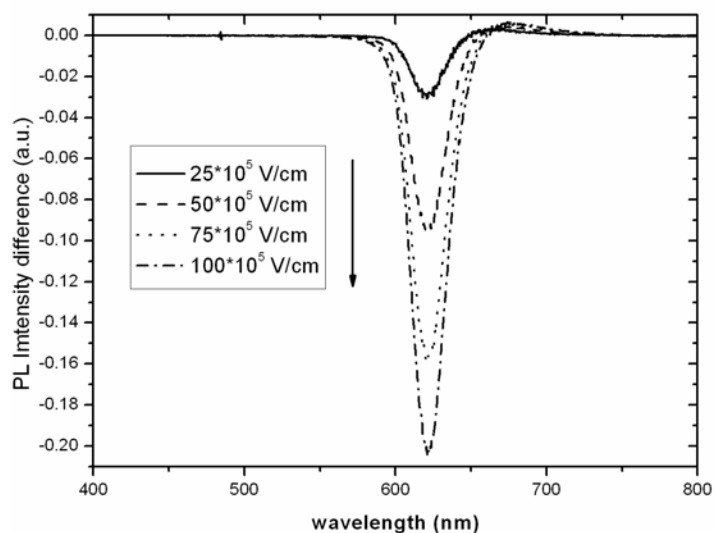
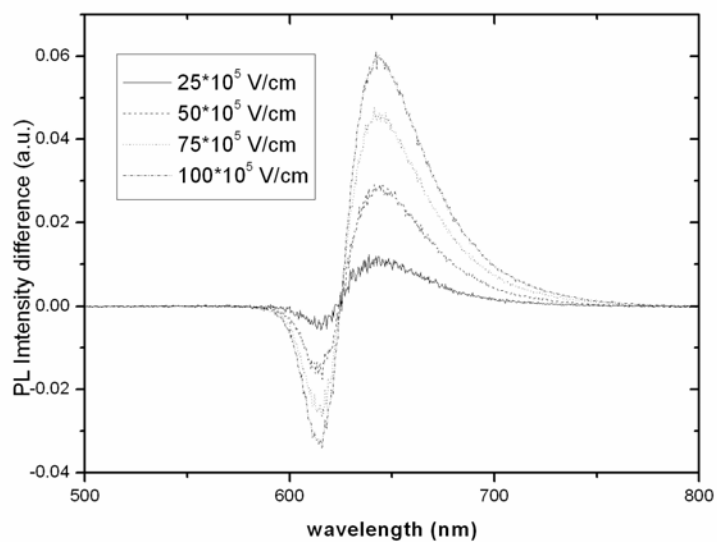


**Figure 3.2.3. 1** Photoluminescence spectra of CdSe nanorods film under different applied voltages. Inset shows the integrated PL intensity vs. the applied electric field.

The spectra in Figure 3.2.3.1 demonstrate the decrease in photoluminescence intensity and red shift with voltage increased. At  $E=10^7$  V/cm the magnitude of PL quenching reaches 20% with respect to the signal measured with no voltage applied (inset). Differential PL spectra at various electric field applied with respect to zero field are shown in Figure 3.2.3.2-(a). Both the negative differential PL signal at  $\lambda=620$  nm (PL quenching) and positive signal at  $\lambda=670$  nm (Stark shift) rise with voltage increase. To demonstrate the Stark shift in PL spectra of the nanorods in strong electric field the differential spectra normalized with respect to zero-field PL spectrum are presented in Figure 3.2.3.2-(b). The character of normalized differential spectra is typical as in previous studies and attributed to the PL quenching and Stark effect [35].



(a)



(b)

**Figure 3.2.3. 2 Differential PL (a) and normalized differential PL (b) spectra of CdSe nanorods parameterized with respect to applied electric field.**

We have also conducted research on the electromodulation of absorption and photoluminescence in CdSe nanodots (quantum dots). In Figure 3.2.3.3, the optical density of CdSe nanodots is shown for different levels of electric field

application. As higher electric field is applied, the exciton peak in the absorption spectrum disappears because of exciton ionization.

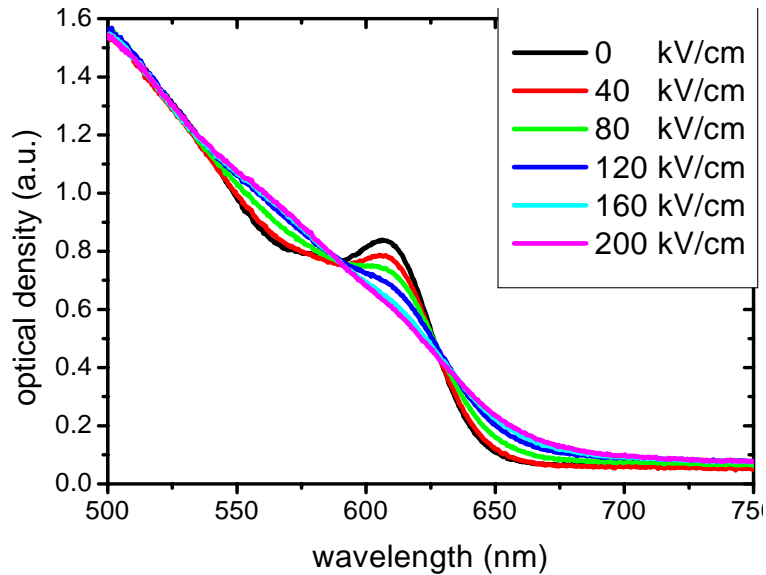


**Figure 3.2.3. 3 Optical density of CdSe nanodots for different electric field values.**

We observe the effects of electric field on photoluminescence, too. As depicted in Figure 3.2.3.4, the photoluminescence quenches about 90% when an electric field of 200 kV/cm is applied around the nanocrystals. This is the highest photoluminescence electromodulation in CdSe nanodots ever reported and it is promising for device applications. Additionally, the luminescence peak is slightly red-shifted as the electric field increases. This arises from the Stark shift. The photoluminescence decreases strongly with applied electric field, which is caused by the decreasing overlap between the electron and hole wavefunctions and eventually exciton ionization at higher electric field values. The red shift is observed because the lowest energy levels in the valance and conduction bands become closer to each other as the electric field increases.

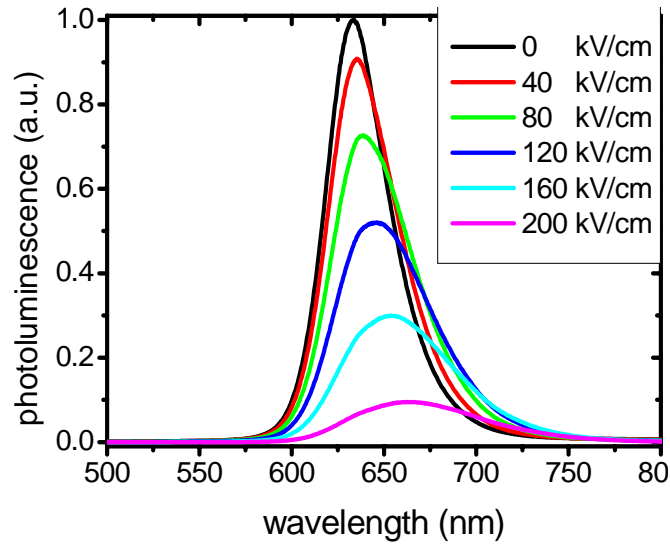


**Figure 3.2.3. 4 Photoluminescence of CdSe nanodots for different electric field values.**

The differential photoluminescence spectrum, which we obtain by subtracting the photoluminescence under zero electric field from the photoluminescence under electric field, also shows the red shift as in Figure 3.2.3.5. Photoluminescence and absorption electromodulation experiments have been conducted with our participation in collaboration with our research partner Institute of Molecular and Atomic Physics of Belarus.

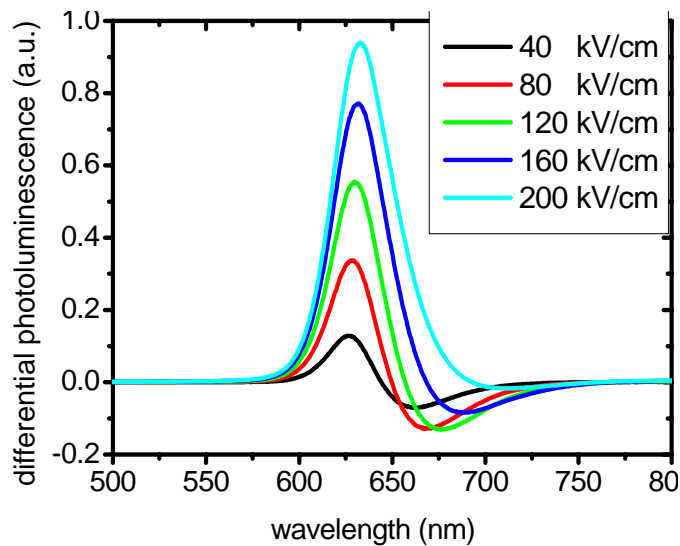


**Figure 3.2.3. 5 Differential photoluminescence spectra of CdSe nanodots under different applied electric fields.**

## **Chapter 4**

# **Localized Plasmon-Coupled Emission of Nanocrystals**

### **4.1 Metal-Enhanced Luminescence**

Metal-enhanced luminescence relies on the idea of enhancing the emission of luminescent (and also fluorescent) materials utilizing surface plasmon polaritons or localized surface plasmons. It has been demonstrated for different materials, including epitaxially grown structures, quantum dots, dyes, and different molecules.

There are 3 basic mechanisms that influence the luminescence of materials close to metal structures, metal films or metal particles: The very high electric field in the near field of the metal, the increased radiative recombination rate of the fluorescent material, which increases the emission intensity, and the resonant energy transfer from the material to the metal, which adds to the nonradiative recombination rate [37]. All mechanisms arise from the increased photon density of states [38].

The very high electric fields around plasmons have been explained and demonstrated in Chapter 2. The reason of increased radiative recombination rate of materials close to plasmons is not as clear as the increased field phenomenon. According to a model named as “radiating plasmon model”, the radiative recombination rate of light-emitting materials close to metals increases because energy is nonradiatively transferred from the excited material to the plasmon modes, which scatters light very efficiently around its resonance wavelength.

Also, the coupling rate between the plasmon modes and the excited fluorescent material is much faster than the nonradiative relaxation processes of the excited material because of the large electromagnetic fields caused by the large photon density of states [39,40]. Therefore, if the scattering of the metal nanoparticles is efficient, the emission can be enhanced. As mentioned in Section 2.2.2.1, the portion of scattering in the extinction cross-section of metal nanoparticles increases with the increasing size, approaching 100% for particles larger than 100 nm. The other contribution to the extinction of metal nanoparticles is the absorption modeled as a loss because it dissipates the energy transferred from the excited material (mostly in the form of heat). This theory is supported by the fact that metal colloids smaller than 20 nm are efficient luminescence quenchers [41]. According to this model, the larger the size of the metal nanoparticle, the better the enhancement is. However, this is not fully correct because the quality of localized plasmon resonance decreases for very large particles. Thus, this trade-off leads an optimal range of metal nanoparticle size for luminescence enhancement. For example, the optimal radius of silver nanoparticles is around 40 nm for metal-enhanced luminescence [42].

The three basic mechanisms in plasmon-influenced light emission, i.e. enhanced electric field, increased radiative recombination rate, and resonant energy transfer, have different dependences on the distance from the metal surface. Quenching is dominant only for distances less than 5 nm between the metal and the nanocrystal because resonant energy transfer decays rapidly with distance. The enhanced electric field becomes negligible for distances larger than approximately 15 nm from the surface of the metal nanoparticle. Increased recombination rate decreases slower than the other mechanisms, and it is valid up to 25 nm from the surface. Figure 4.1.1 compares the evolution of mentioned interactions with distance. As a result of these distance-dependence behaviors, strong enhanced fluorescence is expected for distances about 5-10 nm from the metal nanoparticle surface [43].

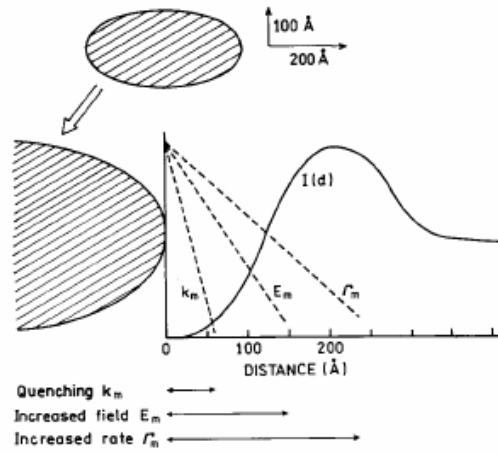


**Figure 4.1. 1 Distance dependence of the three mechanisms (quenching, increased field, and increased rate) caused by metal-luminophore interaction (after [43])**

It is better to quantitatively demonstrate the effects of plasmon on luminescence. The emission enhancement factor in the vicinity of metal nanoparticles is given by:

$$Y = \left| L(\omega_{exc})^2 Z(\omega_{flu}) \right| \quad (4.1.1)$$

where  $L(\omega_{exc})$  is the enhancement factor of the local electric field amplitude at the excitation frequency, and  $Z(\omega_{flu})$  is the increasing factor of quantum yield at the emission frequency [37]. It is defined as

$$Z(\omega_{flu}) = \frac{QY_{metal}}{QY_0} \quad (4.1.2)$$

where  $QY_{metal}$  is the quantum yield with metal and  $QY_0$  is the quantum yield without the metal.

$$QY_0 = \frac{\Gamma}{\Gamma + k_{nr}} \quad (4.1.3)$$

and

$$QY_{metal} = \frac{\Gamma + \Gamma_m}{\Gamma + \Gamma_m + k_{nr}} \quad (4.1.4)$$

where  $\Gamma$  is the radiative recombination rate,  $k_{nr}$  is the nonradiative recombination rate and  $\Gamma_m$  is the additional radiative recombination rate caused by the metal [44]. Here quenching is ignored assuming that the distance between the metal surface and the emitter is larger than 5 nm. According to equation 4.1.4, if the quantum yield of the emitter is already close to 100%, we cannot increase it further because the internal quantum yield cannot be larger than 100%. However, if the internal quantum yield of the emitter is initially very small, very large increases are possible up to the point the quantum yield becomes almost 100%. Another result we obtain from equation 4.1.1 is that matching the plasmon resonance to the excitation wavelength maximizes the enhancement of incident field, and matching the resonance to the emission wavelength maximizes the enhancement of quantum efficiency. If the excitation and emission wavelengths are close to each other, a wavelength between them can give the optimal result.

Also, with changing recombination rates, the lifetime changes from

$$\tau_0 = \frac{1}{(\Gamma + k_{nr})} \quad (4.1.5)$$

to

$$\tau_m = \frac{1}{(\Gamma + \Gamma_m + k_{nr})} \quad (4.1.6)$$

increasing the emission rate by a factor known as Purcell enhancement,

$$F_P = \frac{\Gamma + k_{nr} + \Gamma_m}{\Gamma + k_{nr}} \quad (4.1.7)$$

The presence of plasmons very close to light-emitting materials has a number of influences. As given in equation 4.1.6, the lifetime shortens with plasmonic coupling. Also, the emission intensity can be significantly enhanced or quenched depending on the conditions. Changing lifetime can also change the width of the emission peak through homogeneous broadening. Additionally, in the case of metal-enhanced fluorescence, the photostability of fluorophores usually increases when they are coupled to surface plasmon modes because photochemical reactions usually occur when the material is in excited state [45].

This is one of the most important results of plasmon-coupled emission for fluorophores because their photostability is an important problem.

## 4.2 Metal Nanostructures Preparation

Surface plasmon polaritons and localized plasmons can be obtained using metals designed and fabricated by different methods. Surface plasmon polaritons occur at flat metal surfaces and special techniques such as grating couplers are necessary if roughnesses are not present on the surface. Surface plasmon polaritons are out of our research focus, so we have not worked on those techniques experimentally. Localized plasmons occur at metal nanoparticles and nanostructures. Colloidal metal nanoparticles can be produced by chemical techniques such as reduction of  $\text{AgNO}_3$  to obtain silver nanoparticles [46]. Also, metal nanostructures can be fabricated with electron beam lithography. Another type of structure fabricated to obtain localized plasmon resonance is metal island films consisting of randomly distributed and separated islands with nanometer-scale sizes instead of continuous films. In this work, we focus on forming metal island films.

We deposit gold and silver island films by evaporating metal on clean and smooth quartz and glass substrates in a vacuum environment. We keep the evaporation rate very slow around 0.1-0.2 Å/sec, and the mass thickness smaller than 25 nm. For such slow evaporation rates and small mass thicknesses, the metal film is not continuous and flat. Instead, separated nanometer-size islands form on the surface. After the evaporation, the metal films can be annealed to allow for the nanoislands to reorganize. The mass thickness, evaporation rate, annealing temperature and annealing duration are the four main parameters that determine the size and organization of silver nanoislands. Generally, larger mass thicknesses cause the nanoislands to be larger in size. If the mass thickness is too large, though, the film becomes almost completely continuous and does not demonstrate any resonance behavior. Annealing the films after evaporation

causes the nanoislands to be bigger in size and more isolated from each other [47]. Large evaporation rates cause the islands to be less distinguishable and more interconnected with each other, which attenuates the localized plasmon resonance behavior of the silver film [48]. The scanning electron microscope (SEM) images of the metal island films we deposit under different conditions are presented in Figure 4.2.1; these SEM images are consistent with the general metal island film formation characteristics described above.

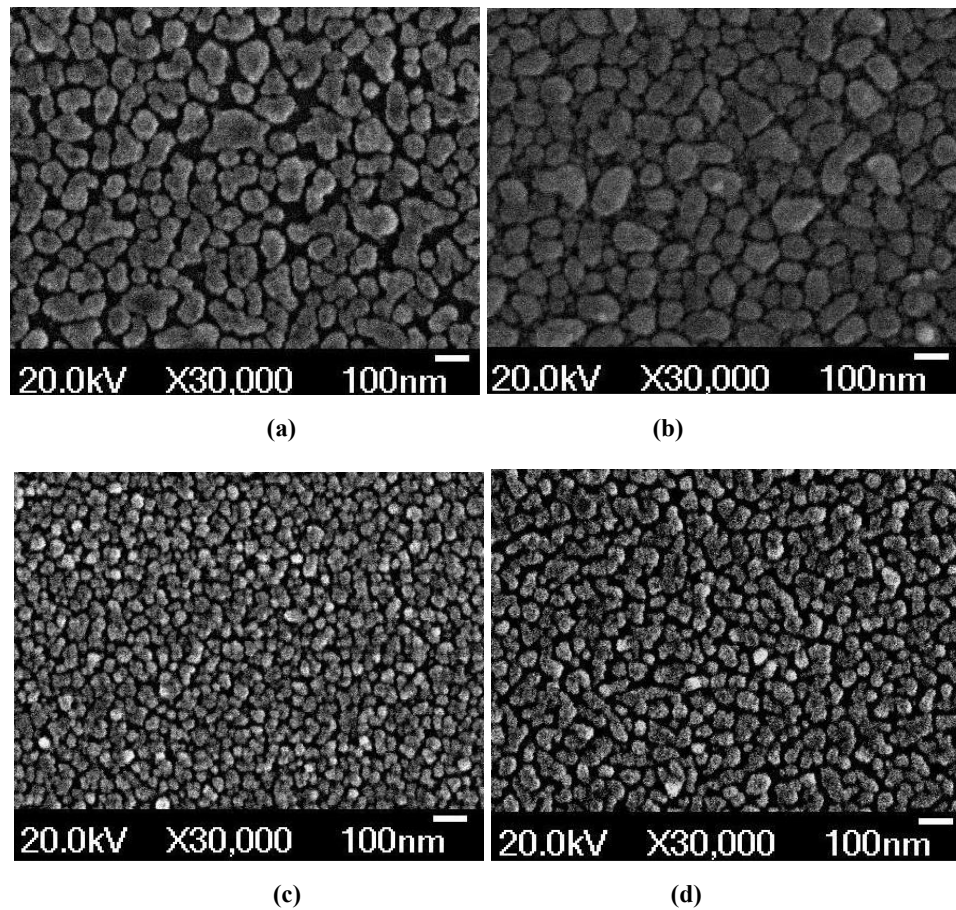


**Figure 4.2. 1** SEM images of our silver nanoisland films: (a) 20 nm mass thickness, not annealed, (b) 20 nm mass thickness, annealed at 300 °C for 10 min., (c) 6 nm mass thickness, annealed at 150°C for 1 min., and (d) 2 nm mass thickness, annealed at 150°C for 2 min.

For the four silver island films depicted in the SEM images, the average nanoisland diameters are listed in Table 4.2.1. As expected, annealing yields

larger and well-separated nanoislands and smaller mass thicknesses lead to smaller nanoislands.

Mass thickness (nm)	Deposition rate ( $\text{\AA}/\text{s}$ )	Annealing temperature ( $^{\circ}\text{C}$ )	Annealing time (min.)	Average nanoisland diameter (nm)
20	0.14	-	-	80
20	0.14	300	10	120
6	0.06	150	1	30
2	0.03	150	2	40

**Table 4.2. 1 Average silver nanoisland diameter for different deposition conditions**

Figure 4.2.2 compares the optical absorption spectra of silver island films prepared with different mass thicknesses, different annealing temperatures, and durations while one film is also covered with 10 nm-thick silicon oxide. The optical absorption peak of the island films comes from the localized plasmon resonance, and the peak wavelength is equal to the resonance wavelength.

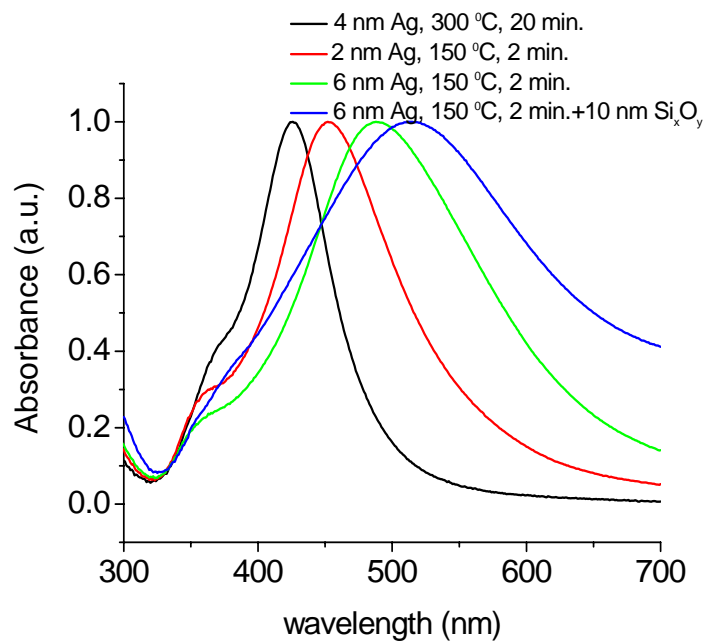


**Figure 4.2. 2 Optical absorption spectra of silver nanoislands with mass thickness of 4 nm annealed at 300°C for 20 min, nano-silver (2 nm) at 150 °C for 2 min, nano-silver (6 nm) at 150°C for 2 min, and nano-silver (6 nm) at 150 °C for 2 min covered with 10 nm thick  $\text{Si}_x\text{O}_y$  film.**

The absorption spectra shown in Figure 4.2.2 provide to be in good agreement with our expectations. Larger mass thicknesses lead to red-shifted plasmon resonance because of the larger nanoislands and sharper plasmon resonance is observed for the metal film annealed at a higher temperature and for a longer time. Also, the existence of silicon oxide layer red-shifts the resonance because the refractive index of silicon oxide is larger than that of air. This characterization proves that the plasmon resonance wavelength of silver island films can be tuned in a broad spectrum range by changing the deposition parameters. Our experiments have shown that this technique is reproducible and we have control over the resonance conditions of silver island films through the mentioned parameters.

We also achieved to obtain plasmon resonance on gold island films. As expected, the resonance wavelength of gold nanostructures is longer than that of silver nanostructures. This expands the spectral range that can be covered even further up to infrared region. We present the optical absorption spectrum of a gold island film with a mass thickness of 4 nm on quartz substrate in Figure 4.2.3. The film was annealed at 300 °C temperature for 10 minutes after evaporation of gold. The resonance wavelength of this sample is 564 nm, and it is possible to get resonance at longer wavelengths by depositing thicker films or annealing at shorter durations with lower temperatures.

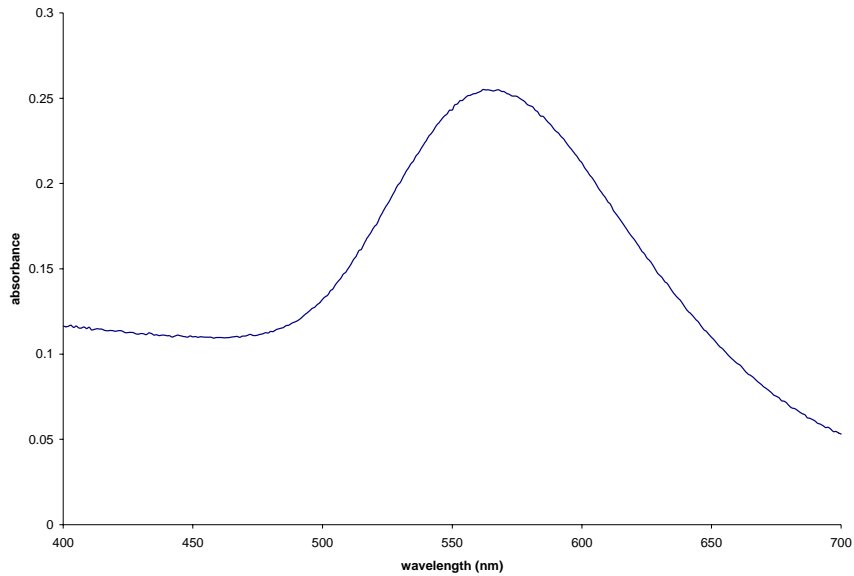


**Figure 4.2. 3 Optical absorption spectrum of a gold island film with a mass thickness of 4 nm annealed at 300 °C for 10 minutes.**

Furthermore, it is possible to obtain resonance wavelengths between those of silver and gold by depositing silver and gold with small mass thicknesses one after the other and annealing afterwards to form islands of silver-gold alloys [49,50]. The resonance wavelength of the alloy can be further tuned by changing the ratio of mass thicknesses of gold and silver. In Figure 4.2.4, the optical absorption spectrum of a silver-gold compound film is presented. The mass thicknesses are 2 nm for both materials, the annealing temperature is 300 °C, and the duration is 10 minutes. Expectedly, we obtain a resonance wavelength of 523 nm, which is between that of silver and gold in similar conditions.

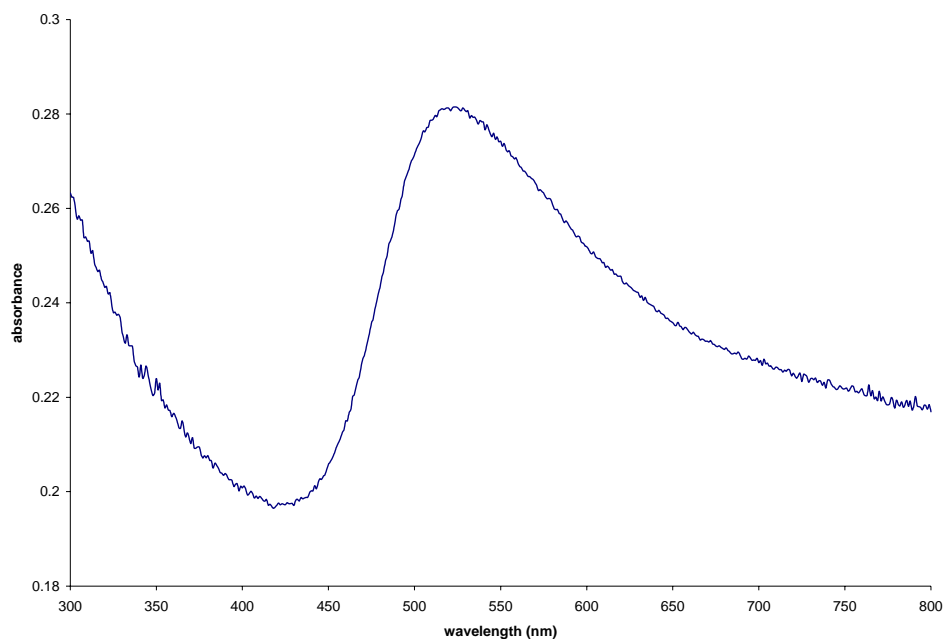


**Figure 4.2. 4 Optical absorption spectrum of a silver-gold alloy metal island film. The mass thicknesses of silver and gold are 2 nm, the annealing temperature is 300 °C, and the annealing duration is 10 minutes.**

We have characterized different metal island films with different mass thicknesses, annealing conditions using different materials such as nanocrystals, polymer, or silicon oxide at the metal interface. Table 4.2.2 lists some of those metal island films with their resonance wavelengths.

Material	Mass thickness (nm)	Annealing temp. (°C)	Annealing duration (minutes)	Material at the interface	Resonance wavelength (nm)
Silver	4	-	-	Free space	446
Silver	4	300	10	Free space	427
Silver	8	150	2	Free space	437
Silver	8	150	2	CdS nanocrystals	498
Silver	10	300	10	Free space	451
Silver	10	300	10	Si <sub>x</sub> O <sub>y</sub>	469
Silver	14	-	-	Free space	474
Silver	14	300	10	Free space	450
Silver	20	300	10	Free space	455
Silver	20	300	10	Si <sub>x</sub> O <sub>y</sub>	476
Gold	4	300	10	Free space	557

Gold	4	300	10	Si <sub>x</sub> O <sub>y</sub>	581
Gold	2	150	1	Free space	591
Gold	2	200	1	Free space	568
Gold	2	200	2	Free space	557
Silver+Gold	2+2	300	10	Free space	523
Silver+Gold	2+2	300	10	PMMA	555

**Table 4.2. 2**Localized plasmon resonance wavelengths of metal island films under different fabrication and measurement conditions.

### **4.3 Experimental Demonstration of Localized Plasmon-Coupled Emission from Nanocrystals**

Using the metal island films we prepare, we experimentally prove that the spontaneous emission characteristics of nanocrystals can be significantly changed when influenced by localized plasmons. The experiments include both CdSe/ZnS core-shell nanocrystals and CdS surface state emitting nanocrystals with different results.

#### **4.3.1 Plasmon-Coupled Emission of CdSe/ZnS Nanocrystals**

Light-emitting devices and biomedical labels are amongst the most important applications of semiconductor nanocrystals and they usually require very high luminescence efficiencies [51,52]. For this, metal-enhanced luminescence is a potential way of obtaining high level of optical emission from semiconductor nanocrystals. Enhancement of luminescence from semiconductor nanocrystals using surface plasmon resonance and localized plasmon resonance has been investigated to date [23,41,53-57]. It has been reported that flat gold films cannot change the luminescence of CdSe/ZnS core-shell nanocrystals even though they enhance the luminescence of CdSe nanocrystals 23-fold [53]. Using gold colloids, luminescence of CdSe/ZnS quantum dots has been increased 5

times [54]. The metal enhanced luminescence of CdSe/ZnS nanocrystals has also been reported with enhancement factors of 30 to 50 using patterned metal nanostructures fabricated with electron beam lithography [23,41]. Another way of plasmon-enhanced luminescence relies on depositing metal island films in the proximity of the luminescent material, and it has been reported for different materials [58]. This method is superior to metal colloids because of higher reproducibility [59]. Also, metal island films are relatively easier to fabricate than patterned metal nanostructures because it does not require advanced fabrication techniques such as electron-beam lithography. In addition to reproducibility and relatively easiness, metal island films have the possibility of controlling the resonance characteristics by changing the deposition conditions as mentioned in the previous section. The use of metal island films to enhance the luminescence of semiconductor nanocrystals has, however, only been reported for CdTe nanocrystals, and a maximum of only 5-fold enhancement has been achieved [57].

Because of this lacking research work on metal island film used to couple with CdSe/ZnS nanocrystals, we fabricate structures to investigate the effects of metal island films on their spontaneous emission properties. In the previous research work on metal-enhanced luminescence of semiconductor nanocrystals (using any type of metal films or structures), mostly the changes in the luminescence intensity have been investigated. However, intensity is not the only important parameter defining the emission of nanocrystals. The peak emission wavelength and the full-width at half-maximum are also important. We investigate the effects of randomly distributed silver island films also on the peak luminescence wavelength and linewidth along with the luminescence intensity of CdSe/ZnS core-shell nanocrystals.

We form closely-packed CdSe/ZnS core-shell nanocrystal films either directly on the nanoislands or on top of a 10 nm thick silicon oxide layer in between them. We grow the silicon oxide layer using plasma-enhanced chemical vapor deposition (PECVD). The reason of using silicon oxide as the dielectric

spacer is its transparency in our operating spectral range. We keep the spacer thickness around 10 nm because it is in the distance range for which quenching is not dominant, and enhancement is optimal. Closely-packed CdSe/ZnS films are formed by drop-casting the nanocrystals in chloroform and evaporating the chloroform in an environment with controlled gas pressure. CdSe/ZnS nanocrystals used in these experiments are 1.9 nm in diameter with a size distribution of  $\pm 5\%$  and a peak emission wavelength of 492 nm. The concentration of nanocrystals is 151 nmol/ml in chloroform.

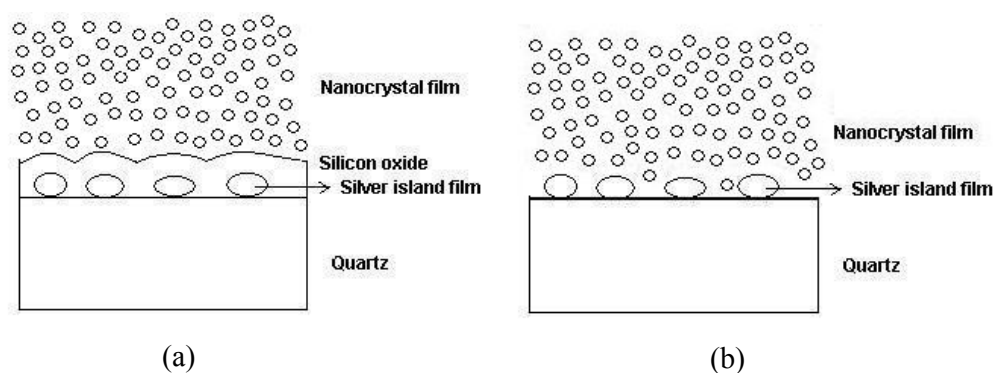


**Figure 4.3.1. 1 Schematic view of the two types of samples prepared: a 10 nm thick silicon oxide film between metal island films and nanocrystals (a), and nanocrystals directly on metal island film (b).**

Matching the plasmon resonance wavelength of silver island films with the emission wavelength of the nanocrystals is important. Additionally, the size of silver nanoislands should not be smaller than 20 nm such that quenching does not dominate. Therefore, we deposit silver island films on quartz with mass thickness of 20 nm with a rate of 0.1 Å/sec, and anneal the resulting film at 300 °C for 10 minutes with nitrogen in the environment. Figure 4.3.1.2 displays the optical absorption spectrum of the prepared silver island films with and without a 10 nm thick silicon oxide layer on the top, along with the emission spectrum of the CdSe/ZnS core-shell nanocrystals to be used for plasmon coupling. The plasmon resonance of the silver island film and emission wavelength of the nanocrystals match very well as depicted in Figure 4.3.1.2. The resonance wavelength is intentionally designed to be slightly shorter than (blue-shifted by

17 nm) the emission wavelength of the nanocrystals so that the red-shift caused later by the addition of the nanocrystal film helps them then match better.

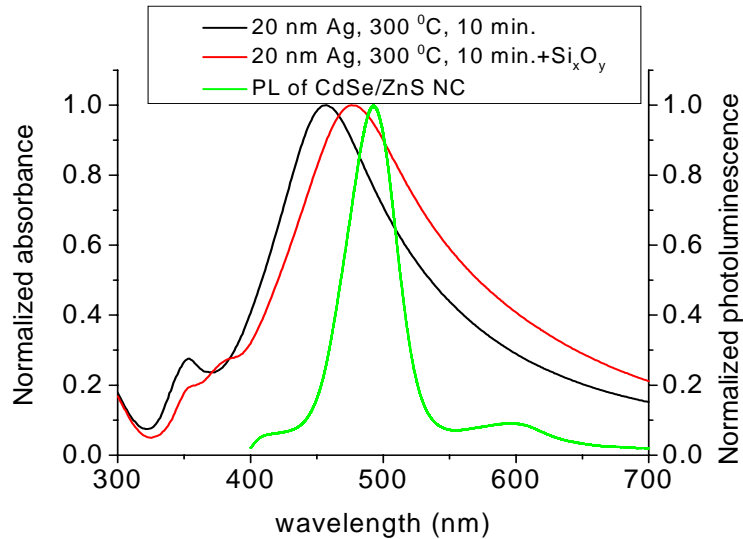


**Figure 4.3.1. 2** Optical absorption spectra of Ag (20 nm) annealed at 300 °C for 10 min and that also covered with 10 nm-thick  $\text{Si}_x\text{O}_y$  along with the photoluminescence spectrum of CdSe/ZnS nanocrystals.

We measure the photoluminescence of our CdSe/ZnS nanocrystals at an excitation wavelength of 325 nm from a He-Cd laser at room temperature. Equal amount of nanocrystals are located on all of the samples under test (including the control groups) under exactly the same conditions. The photoluminescence of the nanocrystals is compared when they are on quartz, on a silver island film, and with a silicon oxide dielectric layer between the nanocrystals and the silver island film. Figure 4.3.1.3 compares the average photoluminescence of the three samples measured under equal conditions. The average photoluminescence is enhanced by 15.1 times when there is a dielectric spacer compared to the case with nanocrystals alone despite the nonuniformity of nanocrystals and metal nanoisland and resulting spatial fluctuation in PL intensity. Also visible from this characterization is that the silver island film quenches the luminescence when the nanocrystals are directly on top of the silver island film. The average photoluminescence drops to 70% of the original value with the influence of

quenching, which makes the average photoluminescence measured with the existence of dielectric spacer around 21.6 times greater than the one without the dielectric spacer. The reader should keep in mind that in this photoluminescence measurement, the excitation wavelength, 325 nm, is far away from the resonance wavelength. Therefore, we cannot benefit from the enhancement of the exciting field in this experiment as well. If the incident light wavelength were close to the resonance, we would expect even larger enhancement of the photoluminescence.

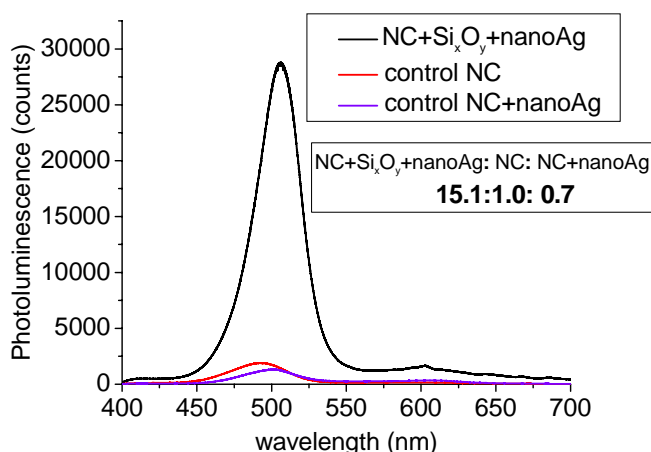


**Figure 4.3.1. 3 Photoluminescence peak intensity of CdSe/ZnS nanocrystals with silver (20 nm) and a dielectric spacer (10 nm silicon oxide) between them is 15.1 times larger than that of the same CdSe/ZnS nanocrystals alone and 21.6 times stronger than that of the same CdSe/ZnS nanocrystals with identical silver nanoislands (20 nm) but no dielectric spacer.**

Additional to the luminescence intensity change, the peak emission wavelength and the linewidth are also affected by the presence of silver island films. Figure 4.3.1.4 emphasizes these changes by comparing the normalized photoluminescence graphs of the two cases, silver island film+Si<sub>x</sub>O<sub>y</sub>+nanocrystals and the nanocrystals alone. The peak emission wavelength shifts from 492 nm to 506 nm and the full width at half maximum decreases from 45 nm to 35 nm with the influence of localized plasmon coupling. We can observe the emission shift not only in enhanced nanocrystals, but also in the quenched ones because both of them are influenced by localized

plasmons. The emission of quenched nanocrystals shifts to 501 nm. We suspect that these luminescence red shifts originate from the interactions between the permanent dipole moments related to the asymmetry of the CdSe/ZnS nanocrystals and the dipole moments created in the silver nanoislands [60].

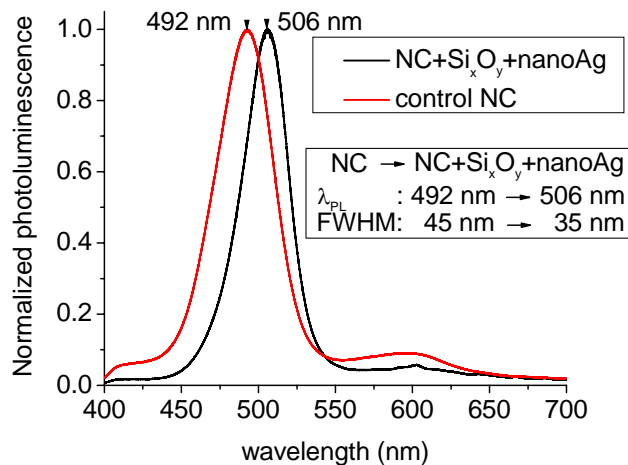
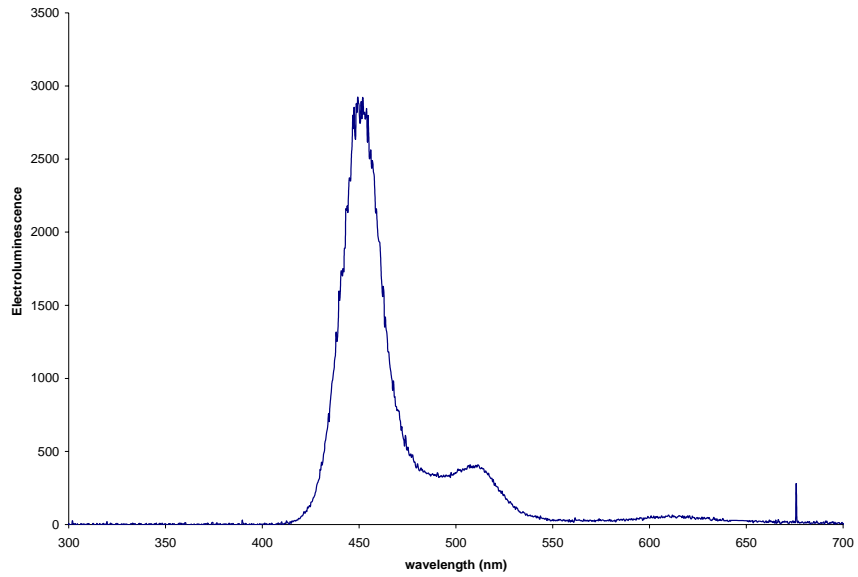


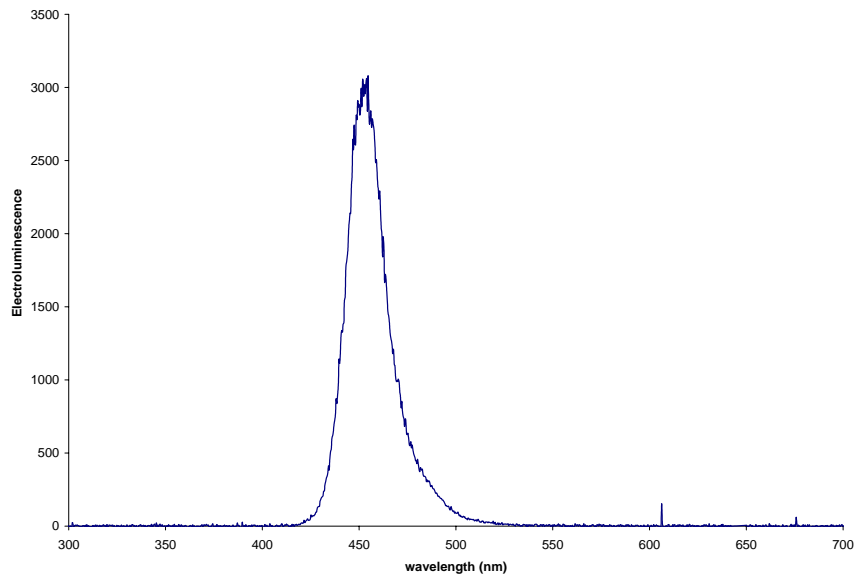
**Figure 4.3.1. 4 Photoluminescence peak wavelength of CdSe/ZnS nanocrystals+Si<sub>x</sub>O<sub>y</sub>+nanoAg (506 nm) is shifted by 14 nm with respect to CdSe/ZnS nanocrystals alone (492 nm) due to plasmonic resonance coupling. Their FWHM linewidth is also narrowed by 10 nm due to the plasmon coupling.**

Finally, we demonstrate the change in the emission of nanocrystals by conducting electroluminescence experiments on our light-emitting diode (LED) grown and fabricated at Bilkent University. The emission wavelength of the LED is 454 nm. Since the emission of LED is used as the exciting radiation, the response of metal-enhanced luminescence is different from the photoluminescence experiment with the He-Cd laser. Nanocrystals are located on the LED, and electroluminescence is measured by driving the LED with a current of 60 mA. In one sample, the nanocrystals are located as in Figure 4.3.1.1-(a) close to a silver island film with a 10 nm thick dielectric spacer in between them, again on the LED. In the other sample, there are not any metal nanostructures. Figure 4.3.1.5 compares the electroluminescence for the two cases. Nanocrystal emission is enhanced significantly even though the LED

emission is absorbed by about 7 dB by the metal film in the first case. Therefore, we believe our approach holds great promise for LED applications.



(a)



(b)

**Figure 4.3.1. 5 Electroluminescence spectrum of the LED with CdSe/ZnS core-shell nanocrystals close to silver island films (a), and of the same sample (with no metal structures) isolated from any plasmon coupling (b).**

### 4.3.2 Plasmon-Engineered Emission of Surface State-Emitting Nanocrystals

Very small-sized CdS nanocrystals act as surface state emitting nanocrystals because emission through the surface states is very significant as a result of the high surface-to-volume ratio. Therefore, their emission spectra span throughout the entire visible spectrum as presented in Figure 4.3.2.1. The peak at 410 nm belongs to interband transitions and emission at longer wavelengths belongs to surface states. Those materials are synthesized with our participation in a collaborative research effort with our research partners at Technical University of Dresden.

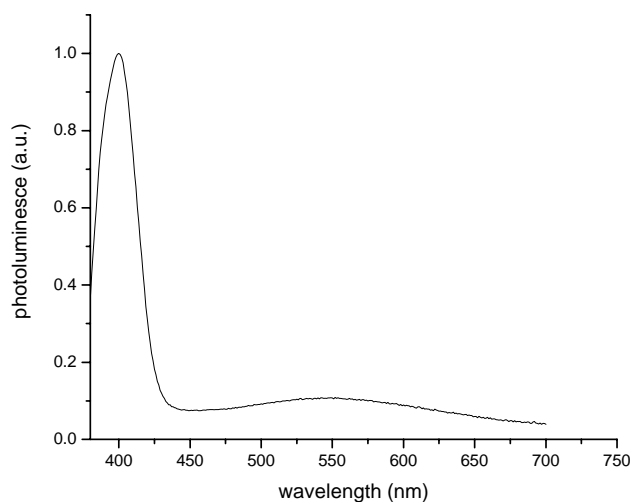


**Figure 4.3.2. 1 Photoluminescence spectrum of surface state emitting CdS nanocrystals.**

We measure the photoluminescence spectra of CdS surface state emitting nanocrystals in the close vicinity of the metal nanoislands and compare the results with the initial spectra. The initial spectrum, which is almost constant excluding the interband transition, changes significantly depending on the resonance conditions of the metal nanoislands. Figure 4.3.2.2 compares the results for surface state emitting nanocrystals without the influence of plasmons,

those in the proximity of a silver island film with mass thickness of 2 nm, and those in the proximity of a gold island film with mass thickness of 2 nm. The results are compatible with our expectations that the resonance wavelength of the gold island film is around 580 nm, and that of the silver island film is around 520 nm, which also appear at the peaks of the enhanced surface state emission. This experiment is very important because it gives us the opportunity to obtain an emission peak at a desired wavelength by only changing the plasmonic metal structure for the same luminescent material.

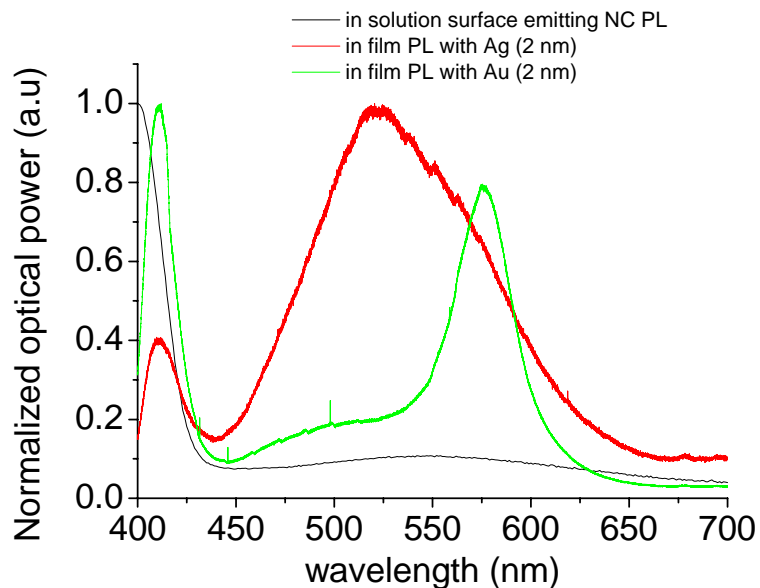


**Figure 4.3.2. 2 Photoluminescence spectrum of surface state emitting nanocrystals without the influence of plasmons compared with those of the same material close to silver and gold nanoislands with the plasmonic coupling.**

# Chapter 5

## Conclusion

In this thesis we worked on the optical properties of localized plasmons and semiconductor nanocrystals. We began with the theory of plasmons and explained the response of metal surfaces and metal nanoparticles to electromagnetic radiation. Later, we numerically showed that the electromagnetic responses of metal nanoparticles can be derived by solving Maxwell's equations using the finite-difference time-domain method. With this method, we demonstrated that local electric fields with very high intensities are formed in the visible range of the spectrum around metal nanoparticles with dimensions much smaller than the wavelength.

In the following chapter we first focused on the theory of electron-hole energy states at semiconductor nanocrystals, and discussed that the confinement of electrons and holes in the nanocrystals make major changes in excitonic behavior and cause discretization of energy levels because of discretized kinetic energy of the carriers. We commented on the effects of this energy level structure on the optical transitions and emphasized the significant dependence of emission peak and absorption edge on the nanocrystal size. Later we summarized the processing techniques of semiconductor nanocrystals for our experimental work and presented our experimental results on the optical absorption and photoluminescence spectra, photoluminescence excitation and time-resolved emission measurements of these nanocrystals. We also added our

experimental demonstration of strong electromodulation of photoluminescence in nanodots and nanorods.

In the following chapter we summarized our experimental research results on the localized plasmon-coupled spontaneous emission of semiconductor nanocrystals. First, we explained the basics of metal-enhanced fluorescence and its dependence on different conditions such as plasmon resonance wavelength, internal quantum efficiency of the emitter, excitation wavelength, and distance between the metal and the emitters. After that, we summarized our experimental method of metal nanostructure fabrication and demonstrated the effect of localized plasmon resonance on the optical absorption spectrum of the metal island films. We also compared the resonance characteristics of different metal island films with different mass thicknesses, annealing conditions, and dielectrics at the interface. Using our optimized metal island films, we observed 15.1 times enhancement of the ensemble average of photoluminescence from CdSe/ZnS core-shell nanocrystals compared to the case without the influence of localized plasmons, and 21.6 times enhancement of the photoluminescence compared to the case where the silver island film quenches the emission. In the same experiment, we shifted the peak emission wavelength by 14 nm and resulted with a 22% narrower emission peak. Additionally, we obtained emission peaks at desired wavelengths in the visible region from CdS surface state emitting nanocrystals by locating them close to metal island films with different resonance properties.

Our experimental research on nanoparticles led to the submission of three journal papers, with one of them being published [61-63], preparation of additional three journal papers, and also eleven refereed or invited international conference presentations [64-74]. Also, we have two patent submissions pending.

## BIBLIOGRAPHY

- [1] <http://www-drfmc.cea.fr/spram/NanoX/research1.htm> (2007).
- [2] R. Osovsky, V. Kloper, J. Kolny-Olesiak, A. Sashciuk and E. Lifshitz, "Optical properties of CdTe nanocrystal quantum dots, grown in the presence of Cd<sup>0</sup> nanoparticles," *J. Phys. Chem. C*, vol. 111, 2007, pp. 10841-10847.
- [3] A. Otto, I. Mrozek, H. Grabborn and W. Akemann, "Surface-enhanced Raman scattering," *J. Phys.: Condens. Matter*, vol. 4, 1992, pp. 1143-1212.
- [4] T. Y. F. Tsang, "Surface-plasmon-enhanced third-harmonic generation in thin silver films," *Opt. Lett.*, vol. 21, no. 4, 1996, pp. 245-247.
- [5] H. Kano and S. Kawata, "Two-photon-excited fluorescence enhanced by a surface plasmon," *Opt. Lett.*, vol. 21, no. 22, 1996, pp. 1848-1850.
- [6] C. D. Geddes and J. R. Lakowicz, "Metal-enhanced fluorescence", *J. Fluoresc.*, vol. 12, no. 2, 2002, pp. 121-129.
- [7] V. M. Agranovich and D. L. Mills, *Surface Polaritons: Electromagnetic Waves at Surfaces and Interfaces*, North-Holland, Amsterdam, 1992.
- [8] C. J. Powell and J. B. Swan, "Effect of oxidation on the characteristic loss spectra of aluminum and magnesium", *Phys. Rev.*, vol. 118, no. 3, 1960, pp. 640-643.
- [9] S. Kawata (Ed.), *Near-Field Optics and Surface Plasmon Polaritons*, Springer-Verlag, Berlin, 2001.

- [10] K. Sönnichsen, *Plasmons in Metal Nanostructures*, Ludwig-Maximilians University of Munich, 2001.
- [11] H. Raether, *Surface Plasmons on Smooth and Rough Surfaces and on Gratings*, Springer-Verlag, Berlin, 1988.
- [12] A. V. Zayats and I. I. Smolyaninov, "Near-field photonics: surface plasmon polaritons and localized surface plasmons," *J. Opt. A: Pure Appl. Opt.*, vol. 5, 2003, S16-S50.
- [13] G. Mie, "Considerations on the optic of turbid media, especially colloidal metal sols," *Ann. Phys.*, vol. 25, 1908, pp. 377-442.
- [14] K. L. Kelly, E. Coronado, L. L. Zhao and G. C. Schatz, "The optical properties of metal nanoparticles: the influence of size, shape, and dielectric environment," *J. Phys. Chem. B*, vol. 107, 2003, pp. 668-677.
- [15] M. Osawa and M. Ikeda, "Surface-enhanced infrared absorption of p-nitrobenzoic acid deposited on silver island films: contributions of electromagnetic and chemical mechanisms," *J. Phys. Chem.*, vol. 95, 1991, pp. 9914-9919.
- [16] S. Link and M. A. El-Sayed, "Size and temperature dependence of the plasmon absorption of colloidal gold nanoparticles," *J. Phys. Chem. B*, vol. 103, 1999, pp. 4212-4217.
- [17] P. B. Johnson and R. W. Christy, "Optical constants of the noble metals," *Phys. Rev. B*, vol. 6, no. 12, 1972, pp. 4370-4379.
- [18] W. A. Murray, S. Astilean and W. L. Barnes, "Transition from localized surface plasmon resonance to extended surface plasmon-polariton as

metallic nanoparticles merge to form a periodic hole array,” *Phys. Rev. B*, vol. 69, 2004, 165407.

- [19] G. C. Schatz, “Theoretical studies of surface enhanced Raman scattering,” *Acc. Chem. Res.* vol. 17, 1984, pp. 370-376.
- [20] F. Tam, G. P. Goodrich, B. R. Johnson and N. J. Halas, “Plasmonic enhancement of molecular fluorescence,” *Nano Letters*, vol. 7, no.2, 2007, pp. 496-501.
- [21] K. R. Catchpole, S. Pillai and K. L. Lin, “Novel applications for surface plasmons on photovoltaics,” Proc. 3<sup>rd</sup> World Conference on Photovoltaic Energy Conversion, Osaka, Japan, 2003.
- [22] M. Futamata, Y. Maruyama and M. Ishikawa, “Local electric field and scattering cross section of Ag nanoparticles under surface plasmon resonance by finite difference time domain method,” *J. Phys. Chem. B*, vol. 107, 2003, pp. 7607-7617.
- [23] P.P. Pompa, L. Martiradonna, A. Della Torre, F. Della Sala, L. Manna, M. De Vittorio, F. Calabi, R. Cingolani and R. Rinaldi, “Metal-enhanced fluorescence of colloidal nanocrystals with nanoscale control,” *Nature Nanotechnology*, vol. 1, 2006, 126-130.
- [24] J. Wessel, “Surface-enhanced optical microscopy,” *J. Opt. Soc. Am. B*, vol. 2, no. 9, 1985, pp. 1538-1541.
- [25] A. Taflove, *Computational Electrodynamics: the Finite-Difference Time-Domain Method*, Artech House, Norwood, 1995.

- [26] A. Taflove, *Advances in Computational Electrodynamics: the Finite-Difference Time-Domain Method*, Artech House, Norwood, 1998.
- [27] G. A. Wurtz, J. S. Im, S. K. Gray and G. P. Wiederrecht, "Optical scattering from isolated metal nanoparticles and arrays," *J. Phys. Chem. B.*, vol. 107, 2003, pp. 14191-14198.
- [28] R. M. Joseph, S. C. Hagness and A. Taflove, "Direct time integration of Maxwell's equations in linear dispersive media with absorption for scattering and propagation of femtosecond electromagnetic pulses," *Optics Letters*, vol. 16, no. 18, 1991, pp. 1412-1414.
- [29] T. Okamoto, I. Yamaguchi and T. Kobayashi, "Local plasmon sensor with gold colloid monolayers deposited upon glass substrates," *Optics Letters*, vol. 25, no. 6, 2000, pp. 372-274.
- [30] S. V. Gaponenko, *Optical Properties of Semiconductor Nanocrystals*, Cambridge University Press, Cambridge, 1998.
- [31] I. Sychugov, *Optical Properties of Nanocrystals*, Royal Institute of Technology, Stockholm, 2006.
- [32] L. Banyai and S. W. Koch, *Semiconductor Quantum Dots*, World Scientific, Singapore, 1993.
- [33] Y. Kayanuma, "Wannier exciton in microcrystals", *Solid State Comm.*, vol. 59, pp. 1986, 405-408.
- [34] G. W. Wen, J. Y. Lin, H. X. Jiang and Z. Chen, "Quantum-confined Stark effects in semiconductor quantum dots," *Phys. Rev. B*, vol. 52, no. 8, 1995, pp. 5913-5922.

- [35] V. L. Colvin, K. L. Cunningham and A. P. Alivisatos, "Electric field modulation studies of optical absorption in CdSe nanocrystals: dipolar character of the excited state," *J. Chem. Phys.*, vol. 101, no. 8, 1994, pp. 7122-7138.
- [36] A. W. Achtstein, H. Karl and Stritzker, "Field induced photoluminescence quenching and enhancement of CdSe nanocrystals embedded in SiO<sub>2</sub>," *Appl. Phys. Lett.*, vol. 89, 2006, 061103.
- [37] T. Nakamura and S. Hayashi, "Enhancement of dye fluorescence by gold nanoparticles: Analysis of particle size dependence," *Jpn. J. Appl. Phys.* vol. 44, no. 9A, 2005, pp. 6833-6837.
- [38] I. Gryczynski, J. Malicka, Z. Gryczynski and J. R. Lakowicz, "Surface plasmon-coupled emission with gold films," *J. Phys. Chem. B.*, vol. 108, 2004, pp. 12568-12574.
- [39] T. D. Neal, K. Okamoto and A. Scherer, "Surface plasmon enhanced emission from dye doped polymer layers," *Optics Express*, vol. 13, no. 14, 2005, pp. 5522-5527.
- [40] K. Okamoto, I. Niki, A. Scherer, Y. Narukawa, T. Mukai and Y. Kawakami, "Surface plasmon enhanced spontaneous emission rate of InGaN/GaN quantum wells probed by time-resolved photoluminescence spectroscopy," *Appl. Phys. Lett.*, vol. 87, 2005, 071102.
- [41] J.-H. Song, T. Atay, S. Shi, H. Urabe and A. V. Nurmikko, "Large enhancement of fluorescence efficiency from CdSe/ZnS quantum dots induced by resonant coupling to spatially controlled surface plasmons," *Nano Letters*, vol. 5, no. 8, 2005, pp. 1557-1561.

- [42] J. R. Lakowicz, "Radiative decay engineering 5: metal-enhanced fluorescence and plasmon emission," *Anal. Biochem.*, vol. 337, 2005, pp. 171-194.
- [43] J. R. Lakowicz, "Radiative decay engineering: biophysical and biomedical applications," *Anal. Biochem.*, vol. 298, 2001, pp. 1-24.
- [44] K. Aslan, I. Gryczynski, J. Malicka, E. Matveeva, J. R. Lakowicz and C. D. Geddes, "Metal-enhanced fluorescence: an emerging tool in biotechnology," *Analytical Biotechnology*, vol. 16, 2005, pp. 55-62.
- [45] C. D. Geddes, H. Cao, I. Gryczynski, Z. Gryczynski, J. Fang and J. R. Lakowicz, "Metal-enhanced fluorescence (MEF) due to silver colloids on a planar surface: potential applications of indocyanine green to in vivo imaging," *J. Phys. Chem. A*, vol. 107, 2003, pp. 3443-3449.
- [46] Y. Sun and Y. Xia, "Shape-controlled synthesis of gold and silver nanoparticles," *Science*, vol. 298, 2002, pp. 2176-2179.
- [47] M. Westphalen, U. Kreibig, J. Rostalski, H. Luth and D. Meissner, "Metal cluster enhanced organic solar cells," *Solar Energy Materials & Solar Cells*, vol. 61, 2000, pp. 97-105.
- [48] G. D. Sockalingum, A. Beljebbar, H. Morjani, J. F. Angiboust and M. Manfait, "Characterization of island films as surface-enhanced Raman spectroscopy substrates for detecting low antitumor drug concentrations at single cell level", *Biospectroscopy*, vol. 4, 1998, S71-S78.
- [49] K. Baba, T. Okuno and M. Miyagi, "Resonance wavelengths of silver-gold compound metal island films," *J. Opt. Soc. Am. B*, vol. 12, no. 12, 1995, pp. 2372-2376.

- [50] K. Baba, T. Okuno and M. Miyagi, "Silver-gold compound metal island films prepared by using a two-step evaporation method," *Appl. Phys. Lett.*, vol. 62, no. 5, 1993, pp. 437-439.
- [51] S. Nizamoglu, T. Ozel, E. Sari and H. V. Demir, "White light generation using CdSe/ZnS core-shell nanocrystals hybridized with InGaN/GaN light emitting diodes," *Nanotechnology*, vol. 18, 2007, 065709.
- [52] D. Alexson, H. Chen, M. Cho, M. Dutta, Y. Li, P. Shi, A. Raichura, D. Ramadurai, S. Parikh, M. A. Stroschio and M. Vasudev, "Semiconductor nanostructures in biological applications," *J. Phys. : Condens. Matter.* vol. 17, 2005, R637-R656.
- [53] K. Okamoto, S. Vyawahare and A. Scherer, "Surface-plasmon enhanced bright emission from CdSe quantum dot-nanocrystals," *J. Opt. Soc. Am. B.* vol. 23, no. 8, 2006, pp. 1674-1678.
- [54] O. Kulakovich, N. Strekal, A. Yaroshevich, S. Maskevich, S. Gaponenko, I. Nabiev, U. Woggon and M. Artemyev, "Enhanced luminescence of CdSe quantum dots on gold colloids," *Nano Lett.* vol. 2, no. 12, 2002, pp. 1449-1452.
- [55] I. Gryczynski, J. Malicka, W. Jiang, H. Fischer, W. C. W. Chan, Z. Gryczynski, W. Grudzinski and J. R. Lakowicz, "Surface-plasmon-coupled emission of quantum dots," *J. Phys. Chem. B.* vol. 109, 2005, pp. 1088-1093.
- [56] K. T. Shimizu, W. K. Woo, B. R. Fisher, H. J. Eisler and M. G. Bawendi, "Surface-enhanced emission from single semiconductor nanocrystals," *Phys. Rev. Lett.* vol. 89, no. 11, 2002, 117401.

- [57] K. Ray, R. Badugu and J. R. Lakowicz, "Metal-enhanced fluorescence from CdTe nanocrystals: a single-molecule fluorescence study," *J. Am. Chem. Soc.* vol. 128, 2006, pp. 8998-8999.
- [58] J. R. M. Kawasaki and S. Mine, "Highly efficient surface-enhanced fluorescence on Ag island film of large pseudotabular nanoparticles," *Chem. Lett.*, vol. 34, no. 7, 2005, pp. 1038-1039.
- [59] V. L. Schlegel and T. M. Cotton, "Silver-island films as substrates for enhanced Raman scattering: effect of deposition rate on intensity," *Anal. Chem.*, vol. 63, 1991, pp. 241-247.
- [60] A. A. Chistyakov, I. L. Martynov, K. E. Mochalov, V. A. Oleinikov, S. V. Sizova, E. A. Ustinovich and K. V. Zakharchenko, "Interaction of CdSe/ZnS core-shell semiconductor nanocrystals in solid thin films," *Laser Physics*, vol. 16, no. 12, 2006, pp. 1625-1632.
- [61] E. Mutlugun, I. M. Soganci and H. V. Demir, "Nanocrystal hybridized scintillators for enhanced detection and imaging on Si platforms in UV," *Optics Express*, vol. 15, no.3, 2007, pp. 1128-1134.
- [62] I. M. Soganci, S. Nizamoglu, E. Mutlugun and H. V. Demir, "Localized plasmon-engineered spontaneous emission of CdSe/ZnS nanocrystals closely-packed in the proximity of silver island films," submitted.
- [63] I. M. Soganci, E. Mutlugun, S. Tek, I. O. Huyal, D. Yucel, G. Celiker and H. V. Demir, "The critical role of particle size and spectral activation conditions in the photocatalysis of titanium dioxide nanoparticles," submitted.

- [64] I. M. Soganci, E. Mutlugun, S. Tek, H. V. Demir, D. Yucel and G. Celiker, "Size effect in optical activation of TiO<sub>2</sub> nanoparticles in photocatalytic process," Proceedings of *IEEE Lasers and Electro-Optics Society 2006 Annual Meeting (LEOS)*, Montreal, QC, Canada (29 October – 2 November 2006). Paper WN4.
- [65] H. V. Demir, I. M. Soganci and E. Mutlugun, "CdSe/ZnS core-shell nanocrystal based scintillators for enhanced detection in UV," Proceedings of *IEEE Lasers and Electro-Optics Society 2006 Annual Meeting (LEOS)*, Montreal, QC, Canada (29 October – 2 November 2006). Paper WN3.
- [66] H. V. Demir, I. M. Soganci, E. Mutlugun, S. Tek and I. O. Huyal, "Photonic devices and systems embedded with nanocrystals," Proceedings of *SPIE Optics East*, Boston, MI (2006). Invited paper.
- [67] H. V. Demir, E. Sari, E. Mutlugun, I. M. Soganci, T. Ozel and S. Nizamoglu, "Photonic functions in UV enabled by in-solution synthesized nanocrystals and epitaxially grown quantum structures," Proceedings of *NanoTX*, Dallas, TX (2006). Invited paper.
- [68] G. Celiker, D. Yucel, E. Mutlugun, I. M. Soganci, S. Tek and H. V. Demir, "Optical efficiency and NOX reduction properties of photocatalytic TiO<sub>2</sub> nanoparticles activated in UV," Proceedings of *PRA World 2nd International Nano Hybrid Coatings Conference 'Developments of the Minute' (PRA 2007)*, Brussels, Belgium (7-8 March 2007). Session Nano Materials: testing and applications. Invited Paper.
- [69] E. Mutlugun, I. M. Soganci, E. Sari, T. Ozel, S. Nizamoglu and H. V. Demir, "Hybrid nanophotonic devices: UV scintillators and visible/UV modulators," 50th IUVSTA Workshop "Toward novel nanostructure-based devices: nanostructured materials fabrications, characterization and

assembly for novel devices”, Dubrovnik, Croatia, (22 October-26 October 2006).

- [70] A. Lutich, S. Gaponenko, M. Artemyev, E. Ustinovich, I. M. Soganci and H. V. Demir, “Electromodulation of Photoluminescence from CdSe Nanorods Film,” Proceedings of *International Conference on Physics, Chemistry, and Applications of Nanostructures (Nanomeeting-2007)*, Minsk, Belarus (22-25 May 2007).
- [71] E. Mutlugun, I. M. Soganci, S. Tek, H. V. Demir, D. Yucel and G. Celiker, “Optical efficiency of self-cleaning TiO<sub>2</sub> nanoparticles activated in UV,” *2007 Nanometa Conference*, Seefeld, Austria (8-11 January 2007).
- [72] H. V. Demir, E. Mutlugun, S. Tek, S. Nizamoglu, I. M. Soganci, E. Sari, T. Ozel, I. O. Huyal, G. Zengin and C. Uran, “Functional Nanophotonic Materials for Hybrid Use in Optoelectronics,” *The 2007 Material Science and Technology Conference and Exhibition, Nanostructured Ceramic Materials, Science and Technology Symposium: Functional Behavior and Characterization of Nanomaterials*, Detroit, Michigan (16-20 September 2007). Invited Paper.
- [73] H. V. Demir, S. Nizamoglu, E. Mutlugun, T. Ozel, I. M. Soganci, S. Tek, I. O. Huyal, E. Sari, G. Zengin and C. Uran, “Hybrid Nanophotonic Approaches for New Functionality,” to appear in the Proceedings of *SPIE Optics East Conference on Optoelectronic Devices: Physics, Fabrication, and Application*, Boston, MI (9-12 September 2007). Invited Paper.
- [74] I. M. Soganci, S. Nizamoglu, E. Mutlugun and H. V. Demir, “Localized plasmon-engineered spontaneous emission of CdSe/ZnS nanocrystals closely-packed in the proximity of Ag nanoislands,” Proceedings of *IEEE Lasers and Electro-Optics Society 2007 Annual Meeting (LEOS)*, Lake Buena Vista, Florida (21-25 October 2007). Paper WN3.